Preprint submitted to EarthArXiv and *Journal of Geophysical Research Solid Earth*

Ophiolite carbonation: Constraints from listvenite core BT1B, Oman Drilling Project

A. Beinlich[1,*], O. Plümper[2], E. Boter[1,2], I. A. Müller[2], F. Kourim[3], M. Ziegler[2], Y. Harigane[4], R. Lafay[5], P. B. Kelemen[6], and the Oman Drilling Project Science Team

[1] The Institute for Geoscience Research (TIGeR), School of Earth and Planetary Sciences, Curtin University, Kent Street, Perth, Australia

[2] Department of Earth Sciences, Utrecht University, Princetonlaan, Utrecht, The Netherlands

[3] Institute of Earth Sciences, Academia Sinica, Academia Road, Nangang, Taipei 11529, Taiwan

[4] Institute of Geology and Geoinformation, Geological Survey of Japan, The National Institute of Advanced Industrial Science and Technology, 1-1-1 Higashi, Tsukuba, Ibaraki 305-8567, Japan

[5] Géosciences Montpellier, Université Montpellier, Place E. Bataillon, 34095 Montpellier, France

[6] Lamont–Doherty Earth Observatory, Columbia University, Palisades, New York, 10964, USA

*Corresponding author: Andreas Beinlich (andreas.beinlich@curtin.edu.au)

Key Points:

- Large-scale carbonation resulted in pervasive replacement of ultramafic rock by the magnesite-quartz-fuchsite (listvenite) assemblage.
- Clumped isotope thermometry indicates carbonation temperatures predominantly between 100°C and 200°C.
- Carbonation textures indicate a transition from non-equilibrium spheroidal growth to near-equilibrium euhedral growth.

Abstract

The widespread occurrence of the quartz–carbonate alteration assemblage (listvenite) in ophiolites indicates that ultramafic rock represents an effective sink for dissolved CO_2. However, the understanding of the carbonation mechanisms is almost exclusively based on surface samples, which adds significant uncertainty to the interpretation of fossil hydrothermal systems. Here we present novel insight into the reaction textures and mechanisms of ultramafic rock carbonation obtained from the 300 m deep BT1B drill hole, ICDP Oman Drilling Project. Hole BT1B recovered continuous drill core intersecting surface alluvium, 200 meters of altered ultramafic rock comprising serpentinite and listvenite, and 100 meters of the underlying metamorphic sole. The ultramafic part of BT1B is dominated by listvenite with only two thin intercalated serpentinite bands at 90 m and 180 m depth. Microstructural analyses indicate an evolution beginning with non-equilibrium growth of spheroidal carbonate composed of interlayered magnesite and dolomite in the completely serpentinized harzburgite, and magnesite and Ca-magnesite in the listvenite. Carbonate spheroids are characterized by sectorial zoning resulting from radially oriented low-angle boundaries. In the listvenite spheroidal carbonate is overgrown by euhedral magnesite indicative of near-equilibrium growth. Carbonate clumped isotope thermometry indicates carbonate crystallization predominantly between 100°C and 200°C. The strong macroscopic brecciation and veining of listvenite indicate that carbonation was facilitated by significant tectonic deformation allowing for infiltration of reactive fluids over an extended duration.

1 Introduction

Alteration of oceanic crust by hydrothermal fluids is the primary driver of hydrosphere–lithosphere volatile exchange and has significant consequences for rock physical properties and planetary-scale element fluxes. Furthermore, natural carbon uptake in thermodynamically stable carbonate in the oceanic lithosphere represents a means for permanently removing CO_2 from the atmosphere (Kelemen & Matter, 2008). The carbon uptake potential is particularly strong in the ultramafic part of the oceanic lithosphere that has previously equilibrated under dry and high temperature conditions and has high concentrations of divalent metal ions, required for carbonate mineral formation (Kelemen et al., 2011). The resulting carbonate minerals are typically Mg-rich (dolomite and magnesite) and accompanied by secondary silicate phases including talc, quartz, and fuchsite (Cr-muscovite) and additional Fe-oxide, -hydroxide and/or sulfide phases. Altered ultramafic rocks consisting of the magnesite–quartz assemblage are termed listvenite and represent the end-product of CO_2-fluid driven mafic and ultramafic rock alteration as almost the entire inventory of Mg and Ca cations is incorporated into carbonate minerals (Halls & Zhao, 1995). Natural carbon uptake in ultramafic formations is significant as evidenced by abundantly exposed carbonate-bearing ophiolite complexes worldwide (Akbulut et al., 2006; Azer et al., 2019; Barnes & O'Neil, 1969; Barnes et al., 1978; Beinlich et al., 2010, 2012, 2018; Belogub et al., 2017; del Real et al., 2016; Emam & Zoheir, 2013; Gahlan Hisham et al., 2018; Halls & Zhao, 1995; Hansen et al., 2005; Hinsken et al., 2017; Launay & Fontes, 1985; Menzel et al., 2018; Quesnel et al., 2013; Tominaga et al., 2017; Tsikouras et al., 2006). One of the largest and most well-explored carbonated ophiolite complexes is the Samail ophiolite in the Sultanate of Oman and the United Arab Emirates (Chavagnac et al., 2013a, b; Clark & Fontes, 1990; Falk et al., 2016; Falk & Kelemen, 2015; Kelemen & Matter, 2008; Lacinska & Styles, 2012; Lacinska et al., 2014; Mervine et al., 2014; Nasir et al., 2007; Neal &

Stanger, 1983, 1985; Paukert et al., 2012; Stanger, 1985; Streit et al., 2012). Listvenite is abundant in the Samail ophiolite and present in the basal section above the underlying metamorphic sole. Earlier work has recognized the occurrence of calcite-, dolomite- and quartz-dominated listvenite containing additional fuchsite ± chlorite ± spinel in the form of discontinuous planar lenses and fault-controlled vein systems (Nasir et al., 2007; Stanger, 1985; Wilde et al., 2002). More recently investigated listvenite from Wadi Mansah is characterized by magnesite as the dominant carbonate mineral consistent with peridotite alteration predominately driven by influx of CO_2 (Falk & Kelemen, 2015). In addition to the carbonated ultramafic basal section, the Samail ophiolite comprises a complete sequence of oceanic lithosphere from the upper mantle through to the continental crust all of which have recently been subject to comprehensive drilling and subsequent analysis of rock core, logging, hydrological and microbial sampling in the course of the Oman Drilling Project (OmanDP) (Kelemen et al., 2014). To better constrain the conditions and reaction pathways driving near-complete peridotite carbonation at large scale, here we present the first results of microstructural investigation and carbonate clumped isotope thermometry on samples recovered from Hole BT1B of the OmanDP. BT1B recovered a 300 m long continuous core across the basal thrust of the Samail ophiolite through 200 m of listvenite and intercalated serpentinite into an additional 100 m of the underlying metamorphic sole. Reaction textures are assessed across scales ranging from hand specimen to the nano-scale to constrain critical reaction parameters and chemical equilibration during natural, large-scale ophiolite carbonation.

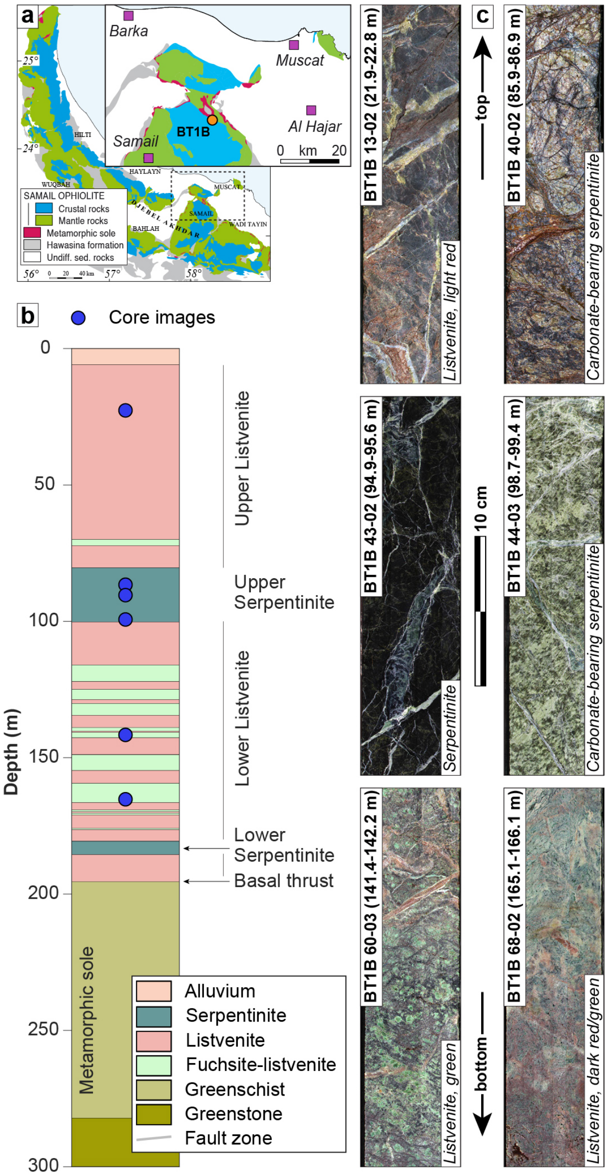

Figure 1 Geological context, down hole stratigraphy and representative core photographs of listvenite core BT1B (Kelemen et al., 2019). **a** Simplified geological map showing the location of Hole BT1B in the context of the regional and local geology (after Nicolas & Boudier, 1995). **b** Downhole stratigraphy of core BT1B showing the relation between listvenite of distinct macroscopic appearance and the presence of relic serpentinite above the basal thrust separating the ophiolite from the underlying metamorphic sole. The blue dots indicate the location of half core photographs shown in Fig. 1c. **c** Representative photographs showing the different macroscopic appearance of listvenite and serpentinite.

2 Geological Setting

The Samail Ophiolite, located in the Sultanate of Oman and the United Arab Emirates, is the most extensive and best-exposed cross-section through the oceanic lithosphere (Fig. 1a). The ophiolite comprises an intact stratigraphy of oceanic crust composed of pelagic allochtonous sediments, overlying pillow basalts and the sheeted dike complex through to gabbro and upper mantle peridotite (Coleman, 1981; Searle & Malpas, 1980). The basal thrust beneath the Samail nappe separates the ophiolite sequence from the underlying metamorphic sole consisting of metasedimentary phyllite, greenschist facies metabasalt and minor amphibolite of the Haybi Complex (Searle & Malpas, 1980). The metamorphic sole is underlain by Permian to Late Cretaceous distal to deep-sea sediments, meta-volcanic rocks, and shelf-facies limestone of the Hawasina Group (Coleman, 1981; Nasir et al., 2007; Searle et al., 2015; Stanger, 1985). Syn- to post-emplacement tectonic tilting of the stratigraphy has been followed by unconformable deposition of Late Cretaceous to Early Miocene transgressive shallow marine sediments prior to Late Miocene to Quaternary uplift and erosion (Coleman, 1981; Searle & Malpas, 1980; Searle et al., 2015).

U–Pb dating of magmatic zircon and ^{40}Ar/^{39}Ar ages of mica and hornblende from the metamorphic sole constrain the timing of thrusting of the Samail ophiolite onto the autochtonous Proterozoic to Mesozoic sedimentary Arabian continental margin between 95 Ma and 80 Ma (Cowan et al., 2014; Gnos, 1998; Hacker, 1994; Hacker & Gnos, 1997; Hacker & Mosenfelder, 1996; Hacker et al., 1996; Lanphere, 1981; Rioux et al., 2012, 2013, 2016; Tilton et al., 1981; Warren et al., 2005). The recently obtained 97±29 Ma Rb–Sr isochron age of listvenite fuchsite, and the fact that listvenites in the Samail ophiolite are only found along the basalt thrust and associated mélange zones, are consistent with syn-emplacement alteration of the ophiolite (Falk & Kelemen, 2015).

3 Materials and Methods

3.1 Macroscopic sample description and context in drill core

Samples used for this study were collected from core BT1B in the course of shipboard core logging aboard D/V Chikyu in September 2017. BT1B was drilled in March 2017 in Wadi Mansah (23°21.861' E, 58°20.149' N), has a total length of 300.1 m, and comprises upper alluvium (2%), serpentinite (8%), listvenite (56%; quartz + carbonate), and the underlying metamorphic sole (34%) (Fig. 1b).

Serpentinite is present in two bands, one between 80 m and 100 m depth (Upper Serpentinite) and another between 181 m and 186 m (Lower Serpentinite) (Fig. 1b). Serpentinite displays a dark green to black color in hand specimen, has a cryptocrystalline grain size, and is typically massive but intersected by abundant veins of light green serpentinite and carbonate (Fig. 1c). Carbonate-rich zones in the Upper Serpentinite occur between 80.54–80.73 m, 81.47–83.63 m and 86.82–88.07 m, and in gradational contacts between serpentinite and listvenite characterized by a distinct increase in carbonate vein abundance and color change to light green. The thickness of these zones ranges from 0.26 m to 3.2 m.

Listvenite is the dominant assemblage in the ultramafic part of BT1B and present as three massive bands between the alluvium and the Upper Serpentinite (6.02 m–80.82 m), between the Upper and Lower Serpentinite (100.2 m–181.3 m) and between the Lower Serpentinite and the basal thrust (185.5 m–196.6 m) (Fig. 1b). Listvenite is cryptocrystalline and macroscopically heterogeneous with frequent color transitions on the centimeter to meter scale between dark and light red, orange, green, tan and pale grey (Fig. 1c). Red and orange listvenite is strongly brecciated in the drill core, and individual clasts show evidence for repeated brecciation and re-cementation such as truncation of clast-hosted veins at clast–matrix boundaries. Pale grey, tan and green listvenite are characterized by the presence of cm-sized quartz–fuchsite intergrowths situated in a pale to dark grey matrix. Tan, pale grey and green listvenite are mainly present between the Upper and Lower Serpentinite, are massive, and locally show foliation resembling ductile deformation.

The basal thrust (196.6 m–197.1 m) is developed as strongly foliated lower part of the lower listvenite unit and upper part of the underlying metamorphic sole separated by 0.42 m of brown to grey–green fault gouge. The metamorphic sole is composed of intercalated, foliated, cryptocrystalline grey–green metabasalt and mafic metasediments. Hole BT1B did not reach the base of the metamorphic sole, but a recent review (Soret et al., 2017) reports that its thickness throughout the ophiolite "is commonly 10–100 m and does not exceed 500 m". Falk & Kelemen (2015) report bulk compositions and Sr isotope ratios for phyllites and carbonates from the underlying Hawasina formation in outcrop within a few kilometers of Hole BT1B.

The study presented here is based on six serpentinite samples from the Upper Serpentinite and nine listvenite samples consisting of light red, dark red and green listvenite from the Upper and Lower Listvenite (Fig. 1).

3.2 Carbonate micro-sampling for stable isotope analyses

A subset of samples was micro-sampled for carbonate stable isotope analysis ($\delta^{13}C$, $\delta^{18}O$) and clumped isotope thermometry. This sample subset includes matrix and vein magnesite, vein dolomite from the Upper Serpentinite (BT1B 43–02 and 44–03) and listvenite (Fig. 1). The majority of listvenite carbonate samples are from the Lower Listvenite, comprising green, light red and dark red listvenite, plus one additional light red listvenite from the Upper Listvenite. Listvenite matrix carbonate is mainly magnesite except for matrix dolomite from core sections BT1B 72–04 and BT1B 77–03. Listvenite vein dolomite was sampled from the Upper Listvenite (BT1B 32–02) and Lower Listvenite (BT1B 67–04) (see also Fig. S1).

Carbonate was sampled by using a micro drill with 3.8 mm inner diameter and a handheld Dremel tool from thin section billets at sites selected based on the petrography of the respective thin sections. Carbonate samples were further crushed to a fine powder using an agate mortar and pestle prior to the analysis.

3.3 Analytical methods

3.3.1 Electron Microscopy

Electron microscopy was conducted on standard petrographic thin sections using an FEI Verios XHR FE-SEM at the Centre for Microscopy, Characterization and Analysis (CMCA), The University of Western Australia. A working distance of 4 mm and an acceleration voltage of 15 keV was used for BSE imaging. Additional TEM foils were prepared from spheroidal carbonate from serpentinite (BT1B 44–01) and listvenite (BT1B 60–03) by focused ion beam (FIB) milling at Utrecht University and CMCA using a FEI Helios Nanolab G3 CX DualBeam FIB-SEM at CMCA. Subsequent scanning transmission electron microscopy (STEM) imaging and quantitative EDX element mapping was carried out using a FEI Titan G2 80-200 at CMCA and a FEI Talos F200X at Utrecht University. Quantitative mineral compositions and element distribution maps were acquired using the JEOL 8530F FE electron microprobe at CMCA using an acceleration voltage of 15 keV and a focused and 5 μm defocused beam for silicate and carbonate minerals, respectively. The analytical procedure and application of reference materials follow the method described in Beinlich et al. (2018). Thin section phase distribution mapping was conducted using a TESCAN Integrated Mineral Analyser (TIMA) high-resolution Field Emission Scanning Electron Microscope (FESEM) in full liberation mode at the John De Laeter Centre, Curtin University. Operating conditions were 15 keV, 0.8 nA and a working distance of 10 mm.

Crystallographic orientations of dolomite and magnesite in two samples BT1B 44–01 and BT1B 70–01 were measured by indexing Electron Backscatter Diffraction (EBSD) patterns acquired using a Hitachi SU3500 SEM equipped with an Oxford Instruments HKL EBSD Nordlys-Nano detector at the Geological Survey of Japan (GSJ). Before EBSD analysis, the thin sections were polished for several minutes with SYTON fluid using a Buehler VibroMet 2 to remove surface damage. Diffraction pattern acquisition was performed in low-vacuum mode using an accelerating voltage of 15 keV, a working distance of 18 mm, specimen tilt of 70° and step size of 0.5 µm. The orientation data were collected using the AZtec software and processed using the MTEX toolbox in Matlab^{TM}. All index data in this study represent points with a mean angular deviation (MAD) of <1°.

3.3.2 X-ray micro-computed tomography

Visualization of the carbonate spherule distribution in serpentinite sample BT1B 44–01 in three dimensions was done using a Zeiss Versa 520 X-ray microscope at CMCA. The X-ray source operated at 80 keV and 7 W, and a Zeiss high-contrast, low-resolution 4X detector was used, achieving a spatial resolution of ~1.5 µm. The sample used was a hand-drilled 6 mm long and 3.8 mm diameter core from the thin section billet used for petrography. Post-processing of the acquired 3D imaging data was done for a sub-volume of the sample core using the Avizo software, version 9.4.

3.3.3 Stable isotope analysis

Stable isotope analyses were performed at the GeoLab, Utrecht University, The Netherlands. Before isotope analysis, the mineralogy of each sample powder was confirmed by XRD to adjust the duration of acid digestion to either dolomite or magnesite. The carbonate $\delta^{13}C$ and $\delta^{18}O$ values are reported relative to Vienna Pee Dee Belemnite (VPDB).

Dolomite samples were digested in 103% phosphoric acid at 70°C for 20 minutes and the released CO_2 was continuously collected in a liquid nitrogen trap using a Kiel IV carbonate device, coupled to a 253 Plus isotope ratio mass spectrometer (both instruments from Thermo Scientific) and analyzed in Long-Integration Dual-Inlet mode (Müller et al., 2017a; with 600 seconds integration time per aliquot). The weight of individual aliquots of reference materials and unknown samples ranged between 75–95 µg. The analyses were carried out in sequences consisting of 38 to 46 individual aliquots, of which 20 were carbonate reference materials. The reference materials used are ETH-1 ($\delta^{13}C$ = 2.20‰, $\delta^{18}O$ = 6.70‰, Δ_{47} = 0.258), ETH-2 ($\delta^{13}C$ = -10.0‰, $\delta^{18}O$ = -10.0‰, Δ_{47} = 0.256) and ETH-3 ($\delta^{13}C$ = 1.95‰, $\delta^{18}O$ = 7.18‰, Δ_{47} = 0.691) (Bernasconi et al., 2018). Each sample and standard gas was measured against a CO_2 reference gas ($\delta^{13}C$ = -7.25‰, $\delta^{18}O$ = 1.65‰), and each unknown sample was analyzed 10 to 14 times, spread over several measurement days.

Magnesite samples were digested offline, using 10–20 mg solid powder and 1–2 ml 103% phosphoric acid at 100°C for 15–16 hours in individual, sealed vials using a custom-built vacuum line containing a cold trap with liquid nitrogen acetone slush (-96°C) to remove H_2O trace quantities from the CO_2 gas. Each measurement sequence consisted of 6 samples, of which 3 were identically treated carbonate reference materials (ETH-1, ETH-2, ETH-3). Each sample analysis, including reference materials, was replicated 4 to 10 times. In contrast to the dolomite analyses, the magnesite analyses were conducted using the Dual Inlet of a Thermo Fisher Scientific MAT 253 in the traditional way by 8 alternating reference gas-sample gas cycles (208 seconds sample gas integration time per measurement).

Clumped isotope analyses of dolomite are reported as Δ_{47} in the absolute reference frame for 70°C reaction temperature without projecting the values down to 25°C acid digestion temperature due to the uncertainties in the dolomite specific temperature-dependent acid fractionation correction (see Müller et al., 2017b, 2019; Murray et al., 2016). The clumped isotope composition Δ_{47} is the measured abundance of the $^{13}C^{18}O^{16}O$ isotopologue (m/z 47) in the carbonate acid digestion-released CO_2 relative to an abundance that would be expected for a stochastic distribution of all isotopes. The deviation from the stochastic distribution is thermodynamically controlled (Eiler, 2007). The raw signal intensities were corrected for negative pressure baselines derived from the m/z 44 beam in the mass spectrometer following the recipe described in Meckler et al. (2014) and Müller et al. (2017b). We then constructed from the measured raw Δ_{47} values of the three ETH calcite standards and their accepted values an empirical transfer function to convert the raw Δ_{47} values of the unknown samples into the absolute reference frame as described in Bernasconi et al. (2018). For the Δ_{47} temperature estimates of dolomite we used the mineral specific Δ_{47}-temperature calibration of Müller et al. (2019) for 70°C acid digestion temperature. For the dolomite $\delta^{18}O$ values we applied the mineral-specific acid fractionation factor of 1.009926 for acid digestion at 70°C (Rosenbaum & Sheppard, 1986).

In contrast to dolomite, magnesite samples were processed identically to the calcite samples since earlier magnesite clumped isotope studies did not observe any differences in acid fractionations of magnesite and calcite (del Real et al., 2016) and more elaborate studies on the magnesite Δ_{47} acid fractionation do not yet exist. The only published value for the magnesite Δ_{47} acid fractionation (Müller et al., 2017b) may be erroneous due to incomplete isotopic re-equilibration during heating of the magnesite in this study. Thus, we use the calcite Δ_{47}-temperature calibration of Kele et al. (2015) recalculated with the new IUPAC (International Union of Pure and Applied Chemistry) parameters in Bernasconi et al. (2018) to derive our estimates of the carbonate formation temperatures. To transfer the raw Δ_{47} values of the magnesites into the absolute reference frame, we constructed an empirical transfer function from the measured raw Δ_{47} values of all analyzed ETH-1,-2,-3 standards (runs DI-3 to DI-12; Dataset S1) against their accepted values at 70°C acid digestion temperature and applied the recalculated calcite Δ_{47}-temperature calibration of Kele et al. (2015) for 70°C acid digestion temperature (by subtracting an acid fractionation correction factor of 0.062‰ from the intercept of the calibration equation). For the magnesite $\delta^{18}O$ values we applied the acid fractionation factor 1.009178 for acid digestion at 100°C (Das Sharma et al., 2002).

4 Results

4.1 Microtexture and phase composition

4.1.1 Serpentinite

Macroscopic description during core logging aboard D/V Chikyu distinguished “serpentinite” from “ophicarbonate”. However, subsequent microtextural analysis shows that also those samples that were macroscopically described as serpentinite are carbonate-bearing. Thus, samples previously classified as either serpentinite or ophicarbonate samples are grouped in this section. The increase in carbonate content, from the least-carbonated serpentinite to listvenite, is gradational. The distinction between carbonate-bearing serpentinite from listvenite is based on the absence of quartz in serpentinite, and the lack of serpentine in listvenite.

The serpentinite with the smallest proportion of carbonate is dominated by lizardite and chrysotile (see Figs S2 and S3) together with chromite, magnetite, bastite intergrowths after pyroxene, minor carbonate and accessory µm-sized awaruite and lack secondary minerals containing ferric iron, e.g. hematite and goethite. Primary olivine and pyroxene were not found in the investigated samples. Carbonate occurs in veins and as spheroidal grains within the serpentine matrix. Crosscutting relationships indicate that carbonate vein formation was preceded by at least two generations of serpentine veining. Carbonate veins frequently follow or are bent toward earlier serpentine veins and sometimes occur in sub-parallel sets with regular vein spacing of ~130–200 µm (e.g. BT1B 44–03). The veins are composed of dolomite or magnesite or a combination of both. Magnesite veins show in most cases a distinct chemical zonation comprising a Fe-rich central part and Fe-poor outer part at the contact with serpentine (Table S1). The composition of serpentine after primary olivine is identical within the analytical uncertainty between samples BT1B 44–01 and BT1B 44–03. Serpentine formed after orthopyroxene (i.e. bastite) shows slightly lower MgO and higher FeO concentrations (Table S2).

Abundant spheroidal carbonate is observed in serpentinite and ophicarbonate samples BT1B 44–01 and BT1B 43–02, respectively (Fig. 2). These grains are characterized by their spherical shape and consistent grain diameters between 60 µm and 80 µm. BSE imaging and element distribution maps show a distinct chemical zonation consisting of relatively large Mg-rich cores, surrounded by a zone of increased FeO, and thin Ca-rich rims (Fig. 2a). Raman spectroscopy (Fig. S3) confirms that the Ca-rich zone of the spheroidal carbonate in serpentinite samples is dolomite. The chemical zonation is in some grains repetitive and defined by a second spherical dolomite zone (Fig. 2a). The outer rim of the carbonate spheroids is in most cases composed of dolomite and less frequently by a thin rim of magnesite (Fig. 3). Magnesite cores and dolomite rims are near their respective endmember compositions, while the outer magnesite core zones are characterized by FeO concentrations of up to 10 wt% (Fig. 2a). Larger matrix carbonate clusters, composed of amalgamated carbonate spheroids, preserve the described chemical and mineralogical zonation (Fig. 2a). Carbonate spheroids in the serpentinite frequently contain sub-µm sized serpentine inclusions (Fig. 3).

4.1.2 Listvenite

Listvenite samples are dominantly composed of carbonate, quartz, and relic chromite and generally lack precursor serpentine and primary magmatic silicate phases. Red listvenite contains additional fine-grained hematite and potentially goethite intergrown with carbonate and quartz. Matrix carbonate is dominated by magnesite, while carbonate veins are either magnesite or dolomite. Based on their crosscutting relationships, thin, sometimes Fe-oxide-bearing magnesite veins (10–50 µm) represent in most cases the oldest vein generation. They are crosscut by thicker magnesite veins (< 1 mm), followed by quartz and/or quartz–carbonate veins (50–300 µm), and then by dolomite veins (<500 µm). The thicker magnesite veins occasionally contain euhedral

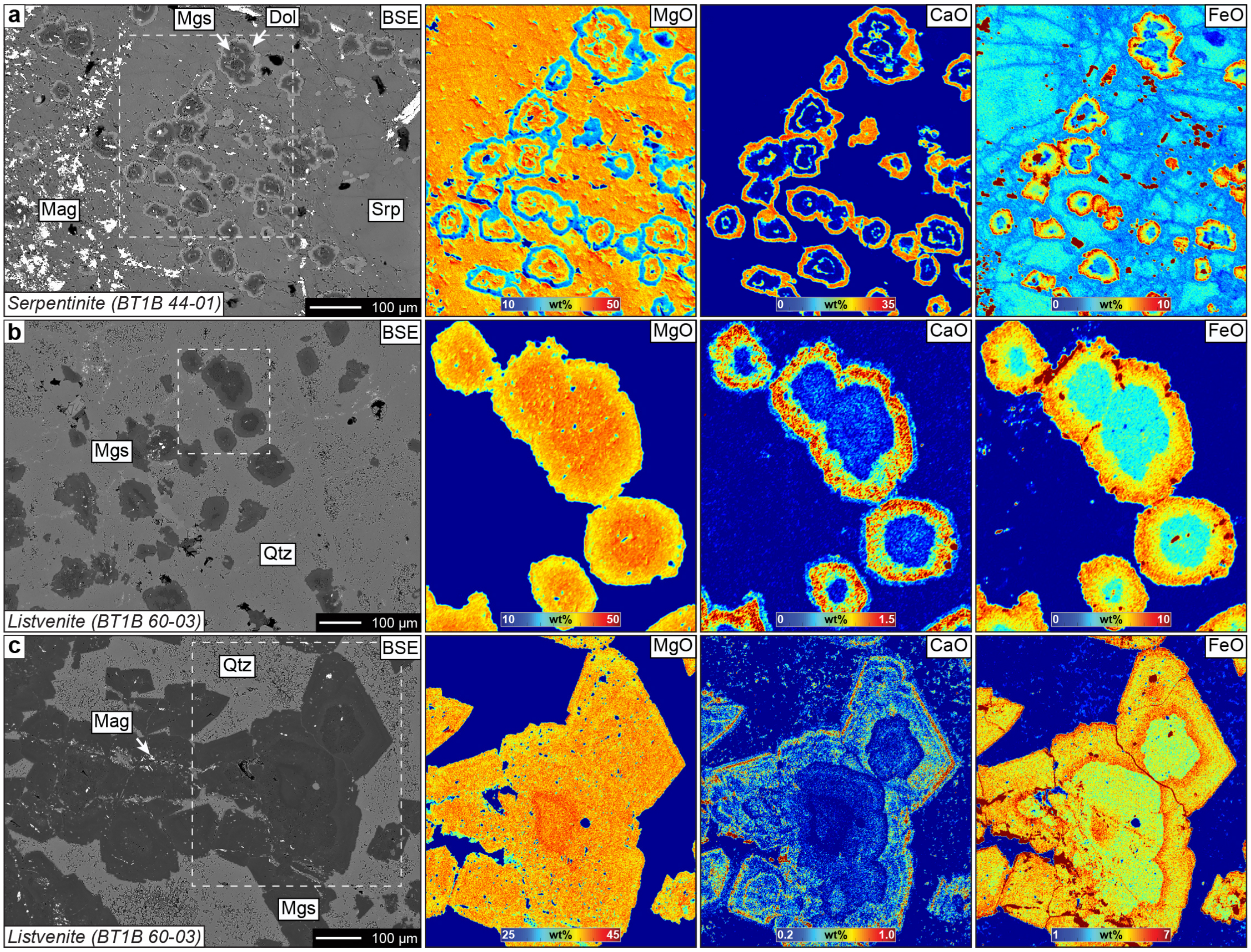

Figure 2 Representative back-scattered electron (BSE) images and quantitative element distribution maps of carbonate in serpentinite and listvenite. **a** Spheroidal magnesite–dolomite composite grains in the least carbonated serpentinite section 44–01. Quantitative element maps showing the chemical zonation of the carbonate. Ca-rich carbonate is identified as dolomite by Raman spectroscopy (not shown), whereas grain core regions are magnesite. FeO enrichment is confined to the magnesite. **b** Spheroidal carbonate in green listvenite core section 60–03. The carbonate growth morphology and chemical zonation is similar to that in serpentinite but Ca-rich carbonate is identified as Ca-magnesite that is also enriched in FeO. **c** Euhedral magnesite in green listvenite section 60–03. The core region of the euhedral magnesite grains resembles the morphology and composition of spheroidal magnesite shown in Fig. 2b.

magnesite showing an oscillatory variation in its Ca content. Additionally, coarse-grained antitaxial magnesite veins frequently show a similar vein-internal chemical zonation as observed in the matrix carbonate spheroids, composed of near-endmember magnesite at the vein-matrix interface as well as high Fe and Ca concentrations in the vein center. Occasionally, thick quartz veins pseudomorph serpentine veins by inheriting their crack-and-seal texture along vein–wall rock interfaces. These are crosscut by a later generation of ~20 µm thin quartz veinlets. Matrix quartz in the listvenite is in most cases cryptocrystalline and shows an interlocked texture. Less frequently, the quartz matrix appears to consist of clusters of sub-µm sized spheroidal quartz, creating an interstitial porosity (BSE images in Fig. 2b and c).

Green listvenite samples (e.g. BT1B 52–01, BT1B 60–03) contain additional fuchsite (Cr-muscovite; Table S2) as intergrowths with quartz and associated with relic chromite. These samples also contain spheroidal carbonate (~80 µm grain diameter) that texturally resembles the matrix carbonate in serpentinite samples. Spheroidal carbonate in the listvenite occurs in the fine-grained quartz

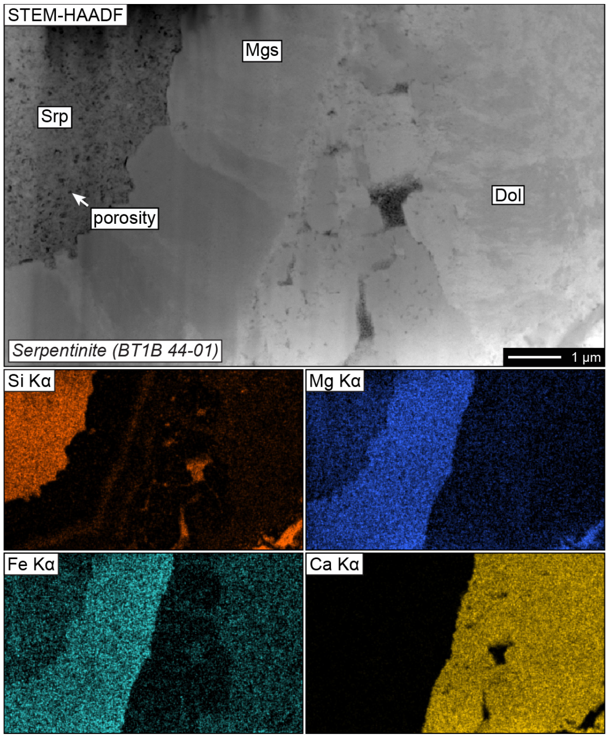

Figure 3 Details of the carbonate–serpentine interface in the least carbonated serpentinite core section 44–01. High angle annular dark-field image (HAADF) acquired in scanning transmission electron microscopy (STEM) mode showing a thin magnesite rim at the interface between the dolomite zone of a spheroidal carbonate and the surrounding serpentine matrix. The element distribution maps highlight the presence of abundant sub-µm serpentine inclusions in carbonate.

matrix as isolated grains and amalgamated clusters of individual spheroids. Listvenite carbonate spheroids also show a systematic compositional zonation with high Mg concentrations in the core and elevated Ca and Fe concentrations in the rim (Fig. 2b). However, the rims are composed of Ca- and Fe-rich magnesite instead of dolomite. Spheroidal magnesite is frequently overgrown by compositionally distinct euhedral magnesite (Fig. 2c). Spheroidal carbonate in the listvenite contains abundant, fine-grained (≤100 nm) spherical silica inclusions, which may be quartz or amorphous silica (Fig. 4).

4.2 Carbonate stable isotope composition and clumped isotope thermometry

Dolomite and magnesite extracted from veins in serpentinite and listvenite, and the listvenite matrix were analyzed for their $\delta^{13}C$ (VPDB), $\delta^{18}O$ (VPDB), and Δ_{47} composition. Δ_{47} values range between 0.275‰ and 0.548‰. The corresponding spread in formation temperatures for all samples is 45±5°C (1σ) to 247±52°C (Fig. 5a; Table S3). Listvenite matrix magnesite formation temperatures range between 52±8°C (BT1B 52–01) and 190±31°C (BT1B 68–02) and listvenite matrix dolomite temperatures between 98±15°C (BT1B 72–04) and 107±19°C (BT1B 77–03) (see also Fig. S1). The dolomite and magnesite veins in the upper serpentinite yielded 227±52°C (BT1B 43–02) and 45±5°C (BT1B 44–03), respectively. In the listvenite, magnesite vein–matrix pairs indicate a higher temperature for the vein (T_{vein}-T_{matrix} = 11°C and 56°C), whereas the matrix magnesite in BT1B 67–04 records a temperature 46°C higher than the vein dolomite in the same sample.

Dolomite $\delta^{13}C$ values range from -2.6‰ to 0.70‰ and magnesite $\delta^{13}C$ values range from -3.8‰ to 0.60‰. Dolomite $\delta^{18}O$ values range from -13.8‰ to -6.2‰ and magnesite $\delta^{18}O$ values range from -9.3‰ to -6.9‰ (Fig. 5b and c; Table S3). In the $\delta^{13}C$ vs. $\delta^{18}O$ space (Fig. 5c), carbonate stable isotope compositions cluster in three groups characterized by equal $\delta^{13}C$ but distinct $\delta^{18}O$, and intermediate $\delta^{18}O$ and low $\delta^{13}C$. Listvenite vein–matrix

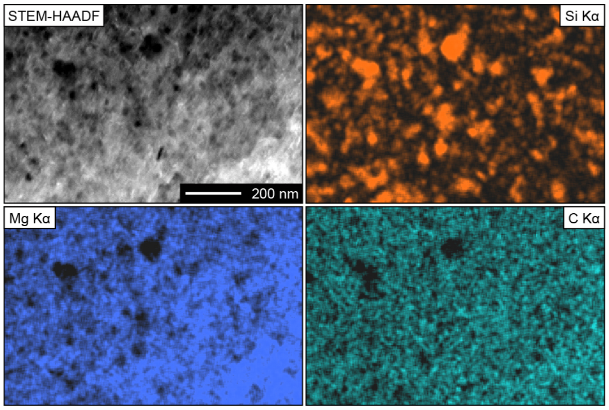

Figure 4 Compositional details (STEM-HAADF) of the core region of a spheroidal magnesite grain in green listvenite section 60–03. The element distribution map indicates the presence of abundant, nm-sized silica inclusions.

magnesite pairs (BT1B 60–03 and BT1B 68–02) show higher matrix δ^{18}O of 0.23‰ and 0.40‰, while δ^{13}C values are 0.26‰ higher and -0.17‰ lower in the matrix compared to the vein. Vein dolomite from BT1B 67–04 has a lower δ^{18}O compared to the matrix magnesite (Δ^{18}O = -5.9‰) but slightly higher δ^{13}C (Δ^{13}C = 0.27‰) (Fig. 5b and c; Table S3).

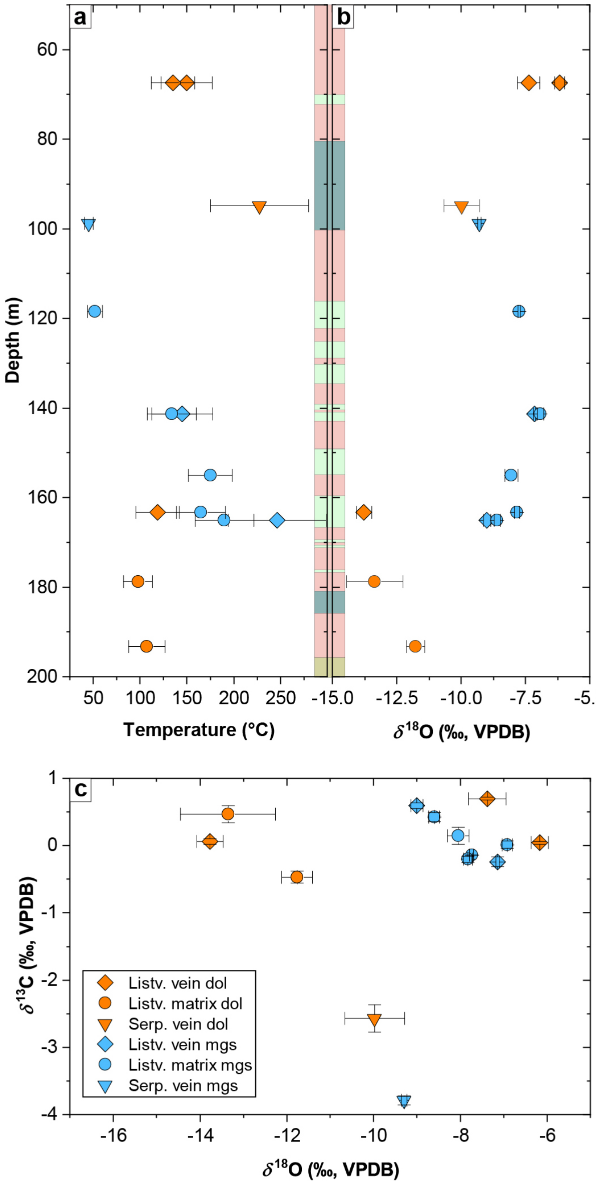

Figure 5 Stable O- and C-isotope systematics. **a** Down-hole plot of clumped isotope carbonate formation temperatures for listvenite and serpentinite samples. Colors and symbols refer to the legend shown in Fig. 5c and differentiate between matrix and vein magnesite and dolomite. The downhole stratigraphy is identical to that shown in Fig. 1. **b** Down-hole plot of magnesite and dolomite δ^{18}O (VPDB). **c** Carbonate δ^{18}O (VPDB) vs δ^{13}C (VPDB) showing clustering at high oxygen and carbon isotope ratios, lower δ^{18}O for some of the listvenite matrix and vein dolomite and lower δ^{13}C for vein dolomite and magnesite from serpentinite sample BT1B 44–01.

5 Discussion

5.1 Incipient carbonation, carbonate nucleation and growth

Conceptually, the per-sample amount of carbonate can be related to reaction progress from incipiently altered serpentinite, containing only some carbonate, to fully carbonated listvenite. Along this conceptual reaction sequence, the carbonate growth texture evolves from isolated spheroids, through clusters of amalgamated carbonate spheroids, to spheroids overgrown by compositionally distinct and euhedral carbonate. The spheroidal carbonate texture in serpentinite (e.g. BT1B 44–03; Fig. 2a) thus represents a snapshot of the incipient carbonation stage. The similar spheroid diameters imply nearly constant rates and durations of nucleation and growth. The presence of abundant carbonate veins, even in the serpentinite, suggests that the initial fluid infiltration was channelized and facilitated by tectonic deformation of the serpentinite host rock. This is further supported by 3D textural analysis showing the existence of smaller veinlets connecting individual carbonate spheroids with larger veins (Fig. 6). However, the 3D textural analysis also shows that a relatively large number of carbonate spheroids occur isolated from carbonate veins. Consequently, further migration of reactive fluid must have occurred by diffusion through interconnected, fluid-filled pore space.

Analyses of TEM dark-field images suggest a porosity of 2.68±1.02% for the serpentinite. The majority of individual pore diameters are less than 100 nm (Fig. 7). At this scale, nanofluidic transport phenomena can be significant and effectively govern metamorphic

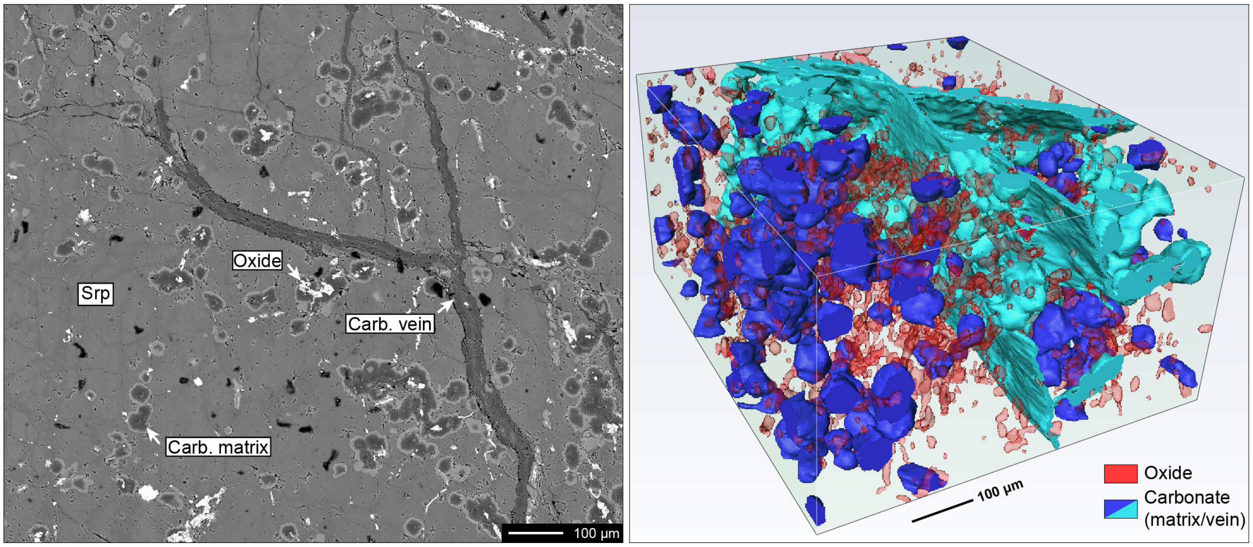

Figure 6 3D reconstruction of X-ray tomography data acquired from the least carbonated serpentinite section 44–01. The BSE image shown on the left side shows an example of the reconstructed texture in two dimensions. The carbonate color code (blue/cyan) highlights connectivity between individual spheroids and the central vein. The pale green, translucent volume is filled by serpentine and omitted for clarity. The reconstructed volume consists of 83.0 vol.% serpentine, 5.4 vol.% isolated carbonate (blue), 8.2 vol.% vein carbonate and connected spheroids (cyan), and 3.4 vol.% oxide phases (magnetite and/or chromite).

fluid-flow, mass transport and hence carbon mineralization (Plümper et al., 2017a; Zheng et al., 2018). These transport phenomena are consistent with the relatively even distribution of carbonate spheroids on the thin section scale (Fig. 8a and b), suggesting that the spatial distribution of carbonate nucleation sites and by implication also the pore fluid saturation state was homogeneous during nucleation. Indeed, the carbonate morphology is in agreement with a strong driving force causing spherical growth instead of sub- to euhedral Mg-carbonate that is frequently observed in similar alteration systems elsewhere (Beinlich et al., 2012; Hansen et al., 2005; Sunagawa, 2005).

Based on the premise that spherulitic growth may result in morphologically similar carbonate and would indicate fast precipitation under far-from-equilibrium conditions (Gránásy et al., 2005; Shtukenberg et al., 2012), we further apply EBSD analysis to representative carbonate spheroids (Fig. 9). This crystallographic examination indicates that spheroidal magnesite is composed of a single crystal and contains abundant, predominantly radial low-angle boundaries (2°–10°) that originate from small dolomite inclusions in the grain centers. High-angle boundaries are exclusively present in the dolomite (Fig. 9a and b). Despite the resemblance with spherulitic carbonate, the fact that carbonate spheroids from BT1B are primarily single crystals is inconsistent with polycrystalline spherulitic growth. Instead, the shape and orientation of such magnesite grains is similar to sector zoning occasionally found in, e.g., garnet and fluorite (e.g., Bosze & Rakovan, 2002; Stowell et al., 2011). Sectorial zoning is commonly related to compositionally distinct zones and ascribed to orientation-dependent differences in crystal growth rates. However, growth competition may also result in crystallographic misfit between adjacent sectors of identical composition, thus forming low-angle boundaries in chemically homogeneous single crystals that are unrelated to external deformation (see also Pearce et al., 2013).

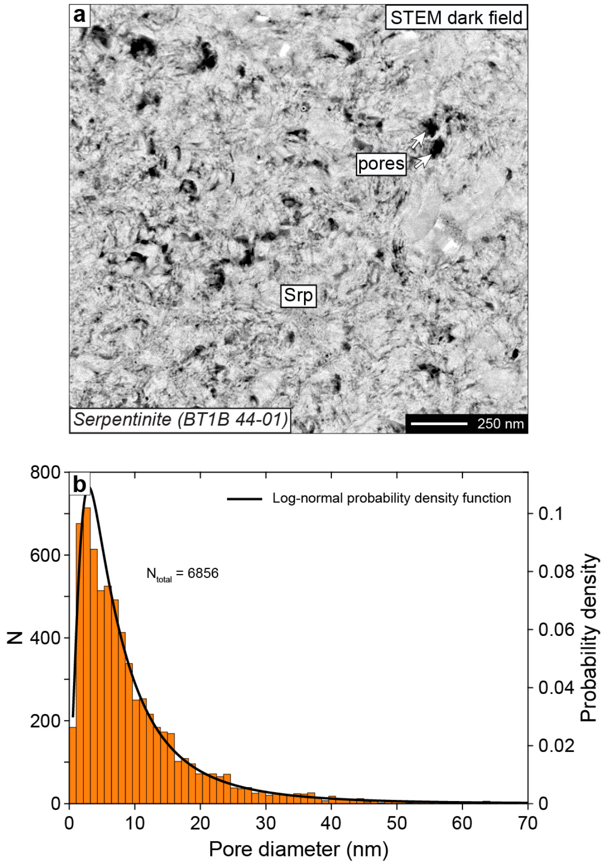

Figure 7 Serpentinite porosity and pore diameter distribution. **a** STEM dark-field image of serpentine in sample BT1B 44–01 shows an example of sub-μm sized porosity. The thresholded porosity of this image is 1.68%. **b** Pore diameter statistics and probability density (PD) based on a log-normal PD fit of the data shown in the histogram. Pore diameter data is based on the analysis of five binarized STEM dark-field images using the maximum entropy threshold in the Fiji distribution of ImageJ (Schindelin et al., 2012).

5.2 Pervasive carbonation and listvenite formation

Listvenite contains spheroidal and euhedral carbonate, both showing a systematic chemical zonation with Mg-rich and Fe- and Ca-poor grain cores, and Fe–Ca-rich rims. Spheroidal magnesite in the listvenite shows a gradual increase in MgO toward the core and a sharp transition to Ca- and Fe-rich magnesite in the rim. Listvenite carbonate spheroids are thus different from those in the serpentinite that show a core to rim increase in FeO and decrease in MgO, and a sharp transition to Fe-free dolomite. Furthermore, listvenite carbonate spheroids contain abundant sub-μm sized silica inclusions (Fig. 4), whereas serpentinite magnesite contains serpentine inclusions (Fig. 3). These characteristics suggest that most of the listvenite carbonate did not evolve from spheroidal carbonate in the serpentinite, but instead formed via direct replacement of serpentine, accompanied by the formation of quartz in the matrix. Nevertheless, EBSD phase- and misorientation-maps show that spheroidal carbonates in the listvenite also consist of magnesite single crystals with radially orientated low-angle boundaries that originate from a central dolomite inclusion (Fig. 9c and d). Thus, we infer that the listvenite carbonate spheroids also precipitated at relatively high supersaturation, resulting in growth competition between adjacent grain sectors and the spheroidal crystal habit.

Assuming that Ca is primarily sourced from the dissolution of clinopyroxene, the low CaO concentration in magnesite rims in the listvenite compared to the serpentinite is likely related to the larger total carbonate amount in the sample (dilution effect). High concentrations of FeO in rims of spheroidal magnesite and the euhedral magnesite overgrowths (Fig. 2b and c) indicate increased availability of Fe during a relatively late stage of listvenite formation. This availability of FeO is attributed to the breakdown of oxide phases (chromite, magnetite, hematite, Fe-oxyhydroxides) in CO_2-rich alteration fluid during listvenite formation, as previously documented for sites in Canada and Norway by Hansen et al. (2005) and Tominaga et al. (2017). Perhaps, this occurred at the same time as crystallization of fuchsite, which formed from reactions involving spinel, silicates and fluid. The transition from spheroidal to euhedral carbonate morphology reflects a driving force reduction during continued crystal growth (Sunagawa, 2005) and may be related to cooling.

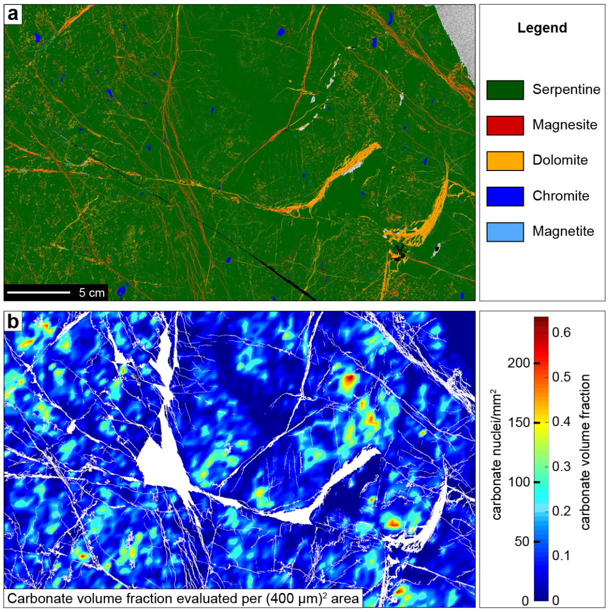

Figure 8 Phase distribution and carbonate nuclei density maps of serpentinite core section BT1B 44–01. **a** High-resolution phase distribution map on the thin section scale showing the relation between spheroidal magnesite–dolomite composite grains, carbonate veins and the serpentine matrix. The relative modal abundances of individual phases are 90.30 vol.% (serpentine), 5.90 vol.% (dolomite), 3.02 vol.% (magnesite), 0.42 vol.% (chromite), and 0.36 vol.% (magnetite). **b** Distribution density map of matrix carbonate evaluated per subsection of 0.16 mm^2 by excluding vein carbonate (white overlay) and using the thresholding routines in the Fiji distribution of ImageJ (Schindelin et al., 2012). The color bar shows both carbonate area fraction and the corresponding number of nucleation sites assuming an average carbonate grain diameter of 60 µm. The distribution of matrix carbonate grains shows clustering that is independent of the location of larger carbonate veins, indicating a relatively constant carbonate saturation state at the thin section scale.

5.3 Carbonation temperature and depth

The clumped isotope distribution in carbonate is thought to be independent of the isotopic composition of the fluid from which the carbonate precipitates (e.g., Eiler, 2007; Ghosh et al., 2006; Huntington et al., 2009), though this is a theoretical prediction that has not been rigorously tested over a broad range in fluid composition and temperature, particularly for dolomite and magnesite. Carbonate clumped isotope signatures can experience solid-state reordering during cooling, depending on the carbonate mineralogy and the cooling rate (Passey & Henkes, 2012). However, dolomite is relatively resistant to solid-state reordering at temperatures below 300°C, thus the temperatures in our study likely reflect the dolomite formation temperatures (e.g. Bonifacie et al., 2017; Ryb et al., 2017). In case of magnesite, solid-state reordering is less well studied. Nevertheless, its sluggish reaction kinetics with phosphoric acid and evidence for an equilibrium blocking temperature of approximately 490°C (del Real et al., 2016) suggest that also the magnesite clumped isotope composition is resistant to isotopic reordering. Hence, we assume that the measured clumped isotope compositions of our carbonate samples reflect their formation temperatures.

The clumped isotope temperatures complement earlier thermometry work in the Samail ophiolite that described relatively low formation temperatures (clumped isotope temperatures between 23–43°C) for young carbonate veins in peridotite forming during present-day weathering (Streit et al., 2012), slightly higher temperatures for calcite veins in peridotite beneath a Cretaceous unconformity (25–60°C, de Obeso & Kelemen, 2018), and yet higher temperatures for carbonate from outcrop samples of listvenite and the metamorphic sole within a few kilometers of Hole BT1B (listvenite 61–114°C, n=15; metamorphic sole 64–171°C, n=4) (Falk & Kelemen, 2015). Also, Falk & Kelemen (2015) documented the presence of intergrown quartz and antigorite, with and without talc and magnesite, in several samples from a gradational contact between listvenite and serpentinite about 2 km north of Hole BT1B. These mineral assemblages equilibrated with a relatively H_2O-rich fluid at temperatures of 80–120°C (depending on the choice of thermodynamic data), broadly consistent with clumped isotope temperatures presented by Falk & Kelemen (2015).

For listvenite carbonate from BT1B analyzed in this study, the clumped isotope data

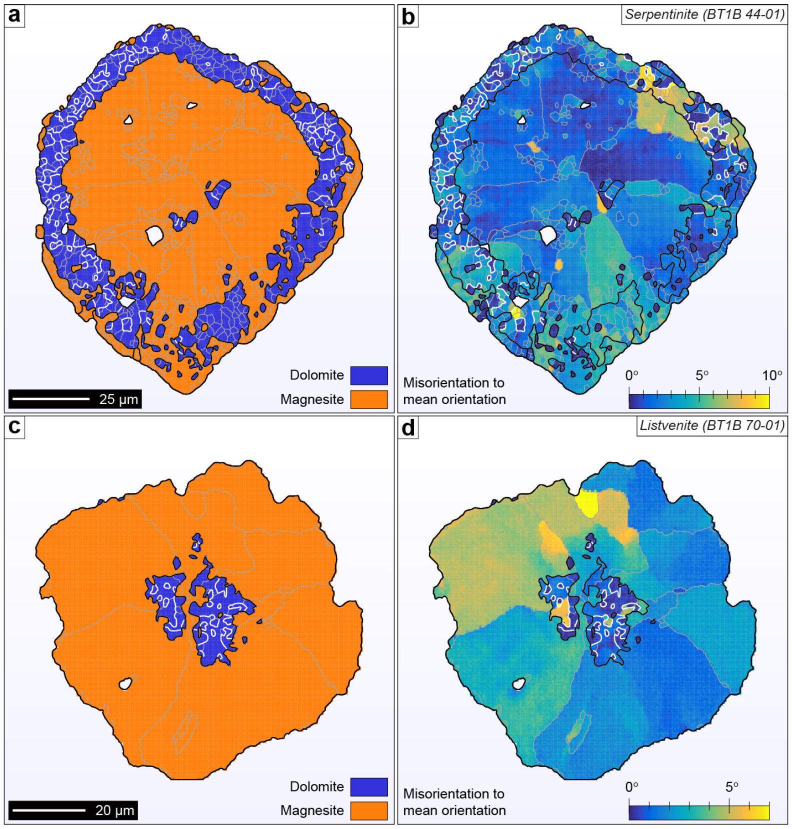

Figure 9 Phase and orientation maps using the Electron Back-Scatter Diffraction (EBSD) system of spheroidal carbonate from the least carbonated serpentinite (BT1B 44–01) and green listvenite (BT1B 70–01). Phase distribution (**a**) and misorientation to mean orientation (**b**) for a magnesite–dolomite composite grain in serpentinite. These data show that the sector zoning of the subgrain orientation may originate at dolomite inclusions near the grain center. Phase distribution (**c**) and misorientation to mean orientation (**d**) maps of spheroidal carbonate in listvenite sample 70–01 are similar to the observations for spheroidal carbonate in serpentinite. Black lines are magnesite–dolomite phase boundaries, and white lines indicate high angle dolomite–dolomite grain boundaries, and grey lines are low-angle (>2 °) sub-grain boundaries in dolomite and magnesite.

yield a relatively wide range of formation temperatures, 52–247°C. In detail, vein dolomite from the red Upper Listvenite formed at ~140°C (67.4 m), whereas matrix magnesite from the Lower Listvenite (118.5 m to 165 m depth) formed between 52–190°C, and listvenite matrix dolomite sampled near the basal thrust (178.7 m and 193.2 m depth) formed at temperatures of 98–107°C. Vein dolomite and magnesite from the relatively narrow Upper Serpentinite yielded one of the highest (227°C) and lowest (45°C) formation temperatures, respectively (Fig. 5; Table S3). Magnesite formation temperatures appear to increase with depth, whereas dolomite formation temperatures are relatively even within the uncertainty except for the high-temperature dolomite vein in the Upper Serpentinite (227°C; BT1B 43–02). Thus, our data show that the overall range in carbonate formation temperatures is wider than previously constrained by carbonate sampled in surface outcrops (Falk & Kelemen, 2015). Furthermore, the relatively erratic temperature distribution throughout core BT1B may reflect that the depth of carbonate formation varied non-systematically with time, consistent with repeated formation of deformation-induced high-permeability pathways allowing reactive fluid infiltration into different structural levels upon cooling of the system.

Assuming that cooling is related to ophiolite obduction, the obtained temperatures can be translated to carbonate formation depth (y), using a simple equation for conductive heat transfer:

$$y = \frac{q_0 - \sqrt{2T_0 Hk\rho - 2Hk\rho T + {q_0}^2}}{H\rho},$$

where q_0 is the surface heat flow (0.06±0.01 $W \cdot m^{-2}$ in forearc settings; Blackwell et al., 1990; Lewis et al., 1988), T_0 is the temperature at the ocean floor (277 K), H is the current mean radioactive heat generation in the mantle (7.42×10^{-12} $W \cdot kg^{-1}$) (Turcotte & Schubert, 2014), k is the thermal rock conductivity (2.9 $W \cdot m^{-1} \cdot K^{-1}$), ρ is the density of partially serpentinized peridotite (2900 $kg \cdot m^{-3}$), and T is the carbonate formation temperature (see also Plümper et al., 2017b).

The calculated depth is mainly dependent on chosen surface heat flow and thermal conductivity values. The 2.9 $W \cdot m^{-1} \cdot K^{-1}$ thermal rock conductivity is based on measurements of serpentinized peridotite from the Mid-Atlantic Ridge (Kelemen et al., 2004), in agreement with the thermal properties of olivine and antigorite (Hofmeister, 1999; Osako et al., 2010). The paleo surface heat flow is unknown but can be constrained based on pressure and temperature conditions of ~850°C and 1 GPa recorded in the metamorphic sole underlying the ophiolite (Agard et al., 2016; Soret et al., 2017). The resulting surface heat flow (0.06±0.01 $W \cdot m^{-2}$) is consistent with these criteria and also with the inferred Permian age of the Samail mantle section and the ~92 Ma mica Ar–Ar ages from the metamorphic sole (Hacker et al., 1996; Jaupart et al., 2015; van Hinsbergen et al., 2019). The resulting geothermal gradient is 25±0.6°C km^{-1}. If our assumptions are correct, then the clumped isotope temperatures place the carbonation depth between ~10.1 km at the highest temperature and 1.7 km at the lowest temperature, thus recording ophiolite uplift of ~8.4 km (Fig. 10; Fig. S4).

5.4 Implications for reactive fluid composition

Ultramafic rock carbonation to listvenite is driven by the infiltration of CO_2-bearing reactive fluid into the ophiolite causing the dissolution of serpentine and precipitation of secondary Ca–Mg and Mg-carbonate and quartz. Primary olivine was not found in core BT1B suggesting that serpentinization went to completion before CO_2-fluid infiltration, while breakdown of relict clinopyroxene may have provided Ca for dolomite growth during incipient carbonation (e.g., in BT1B 44–01). Additional replacement of primary Cr-spinel results in the formation of fuchsite and implies the addition of potassium by the alteration fluid. Similarly altered ultramafic sequences have been described from several other ophiolite occurrences (e.g. Beinlich et al., 2012; Halls & Zhao, 1995; Hansen et al., 2005; Hinsken et al., 2017) and have been the subject of thermodynamic models linking mineral assemblages to fluid composition at given alteration pressure and temperature (Klein & Garrido, 2011; Klein & McCollom, 2013). Thus, we focus here on the implication of measured carbonate formation temperatures.

Assuming that the system had sufficient time to attain isotopic equilibrium between dissolved carbon species, the aqueous fluid, and the precipitating carbonate at the temperatures observed in this study, we can evaluate the fluid $\delta^{18}O$ ($\delta^{18}O_{fluid}$) based on the measured carbonate composition and available temperature-dependent fractionation factors (Aharon, 1988; Chacko & Deines, 2008; Horita, 2014; Matthews & Katz, 1977; Northrop & Clayton, 1966; Schauble et al., 2006; Schmidt et al., 2005; Zheng, 1999). The predicted oxygen isotope fractionation between

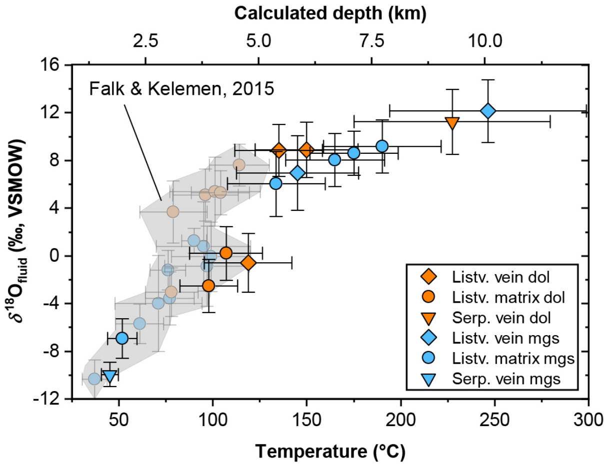

Figure 10 Calculated equilibrium fluid $\delta^{18}O$ (VSMOW) (Aharon, 1988; Horita, 2014) plotted against carbonate clumped isotope temperatures. The secondary abscissa shows depth inferred from the carbonate formation temperatures and simple heat conductivity calculation. The gray shaded area and transparent data point outline the range in fluid $\delta^{18}O$ and temperature based on Falk & Kelemen (2015). Equilibrium fluid $\delta^{18}O$ values calculated using various mineral–fluid oxygen isotope fractionation factors are shown in Fig. S4.

magnesite and fluid ($10^3 \ln\alpha^{\text{Mgs-fluid}}$) varies between 34‰ and 7.8‰ over the temperature range 45–247°C. The strongest fractionation is predicted by Chacko & Deines (2008; magnesite-H_2O) at low temperature (34.9‰), which is distinctly stronger than the predicted fractionation by Zheng (1999) of ~27.3‰. The magnesite-fluid calibration by Aharon (1988; using magnesite 2) yields fractionation factors between 31‰ and 9.5‰ over the same temperature range. For dolomite, the predicted oxygen isotope fractionation varies between 22‰ and 7.2‰ for the temperature range 98–227°C based on the most recent temperature relationship by Horita (2014). In the absence of experimental data on the temperature dependence of magnesite-fluid oxygen isotope fractionation, we here adopt the calibration by Aharon (1988) that is consistent with that by Zheng (1999) and applicable over the investigated temperature range, whereas the magnesite-H_2O equation by Chacko & Deines (2008) is only applicable below 130°C. Furthermore, for oxygen isotope fractionation between dolomite and fluid, we use the calibration by Horita (2014), calibrated over the temperature range 80–350°C. By applying these fractionation factors to the measured oxygen isotope composition of dolomite and magnesite samples that were used for clumped isotope thermometry defines an apparent trend from relatively elevated $\delta^{18}O_{\text{fluid}}$ at a higher temperature (e.g. 12.2‰ at 247°C) to relatively lower $\delta^{18}O_{\text{fluid}}$ at a lower temperature, e.g. -9.9‰ at 45°C. The different calibrations of the oxygen isotope fractionation factors result in a relative variation of $\delta^{18}O_{\text{fluid}}$ of less than 3.7‰ at given temperature (SI Fig. 4; see also del Real et al., 2016).

As previously observed for the area around Hole BT1B (Falk & Kelemen, 2015; their Supplementary Figure 8 and related text), and for low temperature carbonates in altered peridotite worldwide (del Real et al., 2016), the resulting calculated $\delta^{18}O_{\text{fluid}}$ displays a positive correlation with the corresponding carbonate formation temperature (Fig. 10). This correlation may indicate carbonate precipitation from fluids that changed their oxygen isotope ratios and/or were derived from compositionally distinct sources. Low-temperature and low $\delta^{18}O$ fluids may have been sourced from sediment compaction containing seawater-filled pore space during tectonic underthrusting (Falk & Kelemen, 2015; Kelemen et al., 2011), whereas high-temperature fluids with elevated $\delta^{18}O$ may be released by subduction zone devolatilization reactions at the greenschist to amphibolite transition (Menzies et al., 2018). These different fluid sources can be reconciled with the measured carbonate compositions if the seawater $\delta^{18}O$ remained fluid-buffered while trapped in the sedimentary pore space. In addition, recent thermodynamic modelling has shown that magnesite–quartz listvenite assemblage requires fluid CO_2 concentrations of ~2500 ppm, i.e. higher than that of low-pressure fluid saturated with calcite, suggesting that CO_2 was primarily derived from subduction zone devolatilization (de Obeso et al., 2017; Kelemen et al., 2017).

Alternatively, the correlation between carbonate formation temperatures and calculated $\delta^{18}O_{fluid}$ may be unrelated to the fluid composition and instead reflect a tendency toward departure from equilibrium fluid–carbonate oxygen isotope exchange with decreasing temperature. Fluid–mineral oxygen isotope exchange may operate independently from the ordering of clumped isotopes in the carbonate mineral. Further experimental work on the relative rates of isotope exchange and ordering is required to fully investigate the apparent correlation of calculated $\delta^{18}O_{fluid}$ and measured clumped isotope temperatures. However, independently determined fractionation factors (Fig. S4) are mutually consistent despite relative offsets (Fig. S4), and a measurement artifact would be expected to cause a correlation between the measured carbonate clumped isotope composition and $\delta^{18}O_{carbonate}$.

5 Conclusions

Oman DP Hole BT1B intersects 200 m of listvenite containing two intercalated relic bands of the precursor serpentinite. The alteration to listvenite was pervasive, forming an assemblage consisting of Mg- and Ca–Mg-carbonate, quartz, minor fuchsite and in some parts of the core hematite and/or goethite. Precursor olivine and pyroxene minerals could not be found in the serpentinite and listvenite during this study and earlier shipboard core logging. The entire ultramafic part of the core is pervasively veined. Crosscutting relationships in the serpentinite indicate that carbonation was predated by at least two generations of serpentine veining. In the listvenite, crosscutting relationships indicate that early magnesite and minor dolomite veins were followed by a second set of broader magnesite veins, that is cross cut by quartz and quartz–carbonate veins, and then by dolomite veins. Incipient carbonation of the serpentinite matrix resulted in the formation of abundant spheroidal magnesite–dolomite composite grains that show an even spatial and grain size distribution at the thin section-scale and appear to have nucleated on µm-sized, early dolomite. In general, listvenite formation proceeded by the formation of spheroidal magnesite with only minor dolomite in grain cores, followed by precipitation of late euhedral magnesite overgrowths. Both generations of magnesite crystallized together with quartz. However, the listvenite matrix in some parts of BT1B is locally dominated by dolomite instead of magnesite. Fuchsite occurs as fine-grained but relatively large intergrowths with quartz.

Clumped isotope thermometry of selected matrix and vein magnesite and dolomite indicates an overall carbonation temperature range of 45 to 247°C. Carbonate formation temperatures show a weak correlation with depth, indicating that reactive fluid could infiltrate at different structural levels and times. Furthermore, the calculated oxygen isotope composition of the carbonate forming fluid varies between ~-9.9‰ and ~12.1‰ and shows an apparent correlation with temperature. This correlation is consistent with previous observations in Oman (Falk & Kelemen, 2015).

Syn-kinematic deformation facilitated repeated advective fluid infiltration into the ophiolite followed by diffusive transport through the interconnected nano-scale serpentinite pore network. Overall, all observed textures indicate a strong driving force, i.e. equilibrium overstepping for listvenite formation, which may explain the pervasive nature of the alteration and the lack of discernable talc-bearing transitional assemblages between the serpentinite and the listvenite. Late-stage relaxation of the alteration system is reflected by the euhedral habit in relatively low-temperature magnesite in the listvenite. Our observations show that listvenite alteration of ultramafic rock can be significant, pervasive and long-lasting, probably aided by earlier complete serpentinization which reduces the volume strain that would accompany the carbonation of fresh, i.e. olivine-bearing, peridotite.

Acknowledgments

The authors acknowledge the facilities, and the scientific and technical assistance especially by Drs M. Roberts, A. Suvorova and M. Saunders of the Australian Microscopy & Microanalysis Research Facility at the Centre for Microscopy, Characterisation & Analysis, The University of Western Australia, a facility funded by the University, State and Commonwealth Governments. This research used samples and/or data provided by the Oman Drilling Project. The Oman Drilling Project (OmanDP) has been possible through co-mingled funds from the International Continental Scientific Drilling Project (ICDP; Kelemen, Matter, Teagle Lead PIs), the Sloan Foundation-Deep Carbon Observatory (Grant 2014–3–01, Kelemen PI), the National Science Foundation (NSF–EAR–1516300, Kelemen lead PI), NASA–Astrobiology Institute (NNA15BB02A, Templeton PI), the German Research Foundation (DFG: KO 1723/21–1, Koepke PI), the Japanese Society for the Promotion of Science (JSPS no:16H06347, Michibayashi PI; and KAKENHI 16H02742, Takazawa PI), the European Research Council (Adv: no.669972; Jamveit PI), the Swiss National Science Foundation (SNF:20FI21_163073, Früh–Green PI), JAMSTEC, the TAMU–JR Science Operator, and contributions from the Sultanate of Oman Ministry of Regional Municipalities and Water Resources, the Oman Public Authority of Mining, Sultan Qaboos University, CRNS–Univ. Montpellier II, Columbia University of New York, and the University of Southampton. E.B. is grateful for receiving the Olaf Schuiling fond from Utrecht University and A.B.'s participation in shipboard logging was supported by The Institute for Geoscience Research (TIGeR). The clumped isotope analysis by IAM and MZ was funded by the NWO VIDI grant WE.267002.1. TIMA phase mapping was undertaken using the Tescan Mira3 TIMA (ARC LE140100150) at the John de Laeter Centre, Curtin University.

Data availability

Carbonate and silicate mineral compositions and the processed carbonate stable isotope data are available as Supporting Information Tables S1–S3. Analysis results of stable isotope reference materials used to process the unknown samples, and the results of individual analyses of unknown samples will be available online on PANGAEA (www.pangaea.de).

References

Agard, P., Yamato, P., Soret, M., Prigent, C., Guillot, S., Plunder, A., Dubacq, B., Chauvet, A. & Monié, P. (2016). Plate interface rheological switches during subduction infancy: Control on slab penetration and metamorphic sole formation. Earth and Planetary Science Letters, 451, 208-220. https://doi.org/10.1016/j.epsl.2016.06.054.

Aharon, P. (1988). A stable-isotope study of magnesites from the Rum Jungle Uranium Field, Australia: Implications for the origin of strata-bound massive magnesites. Chem Geol, 69(1), 127-145. https://doi.org/10.1016/0009-2541(88)90164-7.

Akbulut, M., Pişkin, Ö. & Karayiğit, A. İ. (2006). The genesis of the carbonatized and silicified ultramafics known as listvenites: a case study from the Mihalıççık region (Eskişehir), NW Turkey. Geological Journal, 41(5), 557-580. https://doi.org/10.1002/gj.1058.

Azer, M. K., Gahlan, H. A., Asimow, P. D., Mubarak, H. S. & Al-Kahtany, K. M. (2019). Multiple stages of carbonation and element redistribution during formation of ultramafic-hosted magnesite in Neoproterozoic ophiolites of the Arabian-Nubian Shield, Egypt. The Journal of Geology, 127(1), 81-107. https://doi.org/10.1086/700652.

Barnes, I. & O'Neil, J. R. (1969). The relationship between fluids in some fresh alpine-type ultramafics and possible modern serpentinization, western United States. GSA Bulletin, 80(10), 1947-1960. https://doi.org/10.1130/0016-7606(1969)80[1947:TRBFIS]2.0.CO;2.

Barnes, I., O'Neil, J. R. & Trescases, J. J. (1978). Present day serpentinization in New Caledonia, Oman and Yugoslavia. Geochim Cosmochim Ac, 42(1), 144-145. https://doi.org/10.1016/0016-7037(78)90225-9.

Beinlich, A., Austrheim, H., Glodny, J., Erambert, M. & Andersen, T. B. (2010). CO_2 sequestration and extreme Mg depletion in serpentinized peridotite clasts from the Devonian Solund basin, SW-Norway. Geochim Cosmochim Ac, 74(24), 6935-6964. https://doi.org/10.1016/j.gca.2010.07.027.

Beinlich, A., Austrheim, H., Mavromatis, V., Grguric, B., Putnis, C. V. & Putnis, A. (2018). Peridotite weathering is the missing ingredient of Earth's continental crust composition. Nat Commun, 9. https://doi.org/10.1038/s41467-018-03039-9.

Beinlich, A., Plümper, O., Hövelmann, J., Austrheim, H. & Jamtveit, B. (2012). Massive serpentinite carbonation at Linnajavri, N-Norway. Terra Nova, 24(6), 446-455. https://doi.org/10.1111/j.1365-3121.2012.01083.x.

Belogub, E. V., Melekestseva, I. Y., Novoselov, K. A., Zabotina, M. V., Tret'yakov, G. A., Zaykov, V. V. & Yuminov, A. M. (2017). Listvenite-related gold deposits of the South Urals (Russia): A review. Ore Geology Reviews, 85, 247-270. https://doi.org/10.1016/j.oregeorev.2016.11.008.

Bernasconi, S. M., Müller, I. A., Bergmann, K. D., Breitenbach, S. F. M., Fernandez, A., Hodell, D. A., Jaggi, M., Meckler, A. N., Millan, I. & Ziegler, M. (2018). Reducing uncertainties in carbonate clumped isotope analysis through consistent carbonate-based standardization. Geochemistry, Geophysics, Geosystems, 19(9), 2895-2914. https://doi.org/10.1029/2017gc007385.

Blackwell, D. D., Steele, J. L., Frohme, M. K., Murphey, C. F., Priest, G. R. & Black, G. L. (1990). Heat flow in the Oregon Cascade Range and its correlation with regional gravity, Curie point depths, and geology. Journal of Geophysical Research: Solid Earth, 95(B12), 19475-19493. https://doi.org/10.1029/JB095iB12p19475.

Bonifacie, M., et al. (2017). Calibration of the dolomite clumped isotope thermometer from 25 to 350°C, and implications for a universal calibration for all (Ca, Mg, Fe)CO_3 carbonates. Geochim Cosmochim Ac, 200, 255-279. https://doi.org/10.1016/j.gca.2016.11.028.

Bosze, S. & Rakovan, J. (2002). Surface-structure-controlled sectoral zoning of the rare earth elements in fluorite from Long Lake, New York, and Bingham, New Mexico, USA. Geochim Cosmochim Ac, 66(6), 997-1009. https://doi.org/10.1016/S0016-7037(01)00822-5.

Chacko, T. & Deines, P. (2008). Theoretical calculation of oxygen isotope fractionation factors in carbonate systems. Geochim Cosmochim Ac, 72(15), 3642-3660. https://doi.org/10.1016/j.gca.2008.06.001.

Chavagnac, V., Ceuleneer, G., Monnin, C., Lansac, B., Hoareau, G. & Boulart, C. (2013a). Mineralogical assemblages forming at hyperalkaline warm springs hosted on ultramafic rocks: A case study of Oman and Ligurian ophiolites. Geochemistry, Geophysics, Geosystems, 14(7), 2474-2495. https://doi.org/10.1002/ggge.20146.

Chavagnac, V., Monnin, C., Ceuleneer, G., Boulart, C. & Hoareau, G. (2013b). Characterization of hyperalkaline fluids produced by low-temperature serpentinization of mantle peridotites in the Oman and Ligurian ophiolites. Geochemistry, Geophysics, Geosystems, 14(7), 2496-2522. https://doi.org/10.1002/ggge.20147.

Clark, I. D. & Fontes, J.-C. (1990). Paleoclimatic reconstruction in northern Oman based on carbonates from hyperalkaline groundwaters. Quaternary Research, 33(3), 320-336. https://doi.org/10.1016/0033-5894(90)90059-T.

Coleman, R. G. (1981). Tectonic setting for ophiolite obduction in Oman. Journal of Geophysical

Research: Solid Earth, 86(B4), 2497-2508. https://doi.org/10.1029/JB086iB04p02497.

Cowan, R. J., Searle, M. P. & Waters, D. J. (2014). Structure of the metamorphic sole to the Oman Ophiolite, Sumeini Window and Wadi Tayyin: implications for ophiolite obduction processes. Geological Society, London, Special Publications, 392(1), 155-175. https://doi.org/10.1144/sp392.8.

Das Sharma, S., Patil, D. J. & Gopalan, K. (2002). Temperature dependence of oxygen isotope fractionation of CO_2 from magnesite-phosphoric acid reaction. Geochim Cosmochim Ac, 66(4), 589-593. https://doi.org/10.1016/S0016-7037(01)00833-X.

de Obeso, J. C. & Kelemen, P. B. (2018). Fluid rock interactions on residual mantle peridotites overlain by shallow oceanic limestones: Insights from Wadi Fins, Sultanate of Oman. Chem Geol, 498, 139-149. https://doi.org/10.1016/j.chemgeo.2018.09.022.

de Obeso, J. C., Kelemen, P. B., Manning, C. E., Michibayashi, K. & Harris, M. (2017), Listvenite formation from peridotite: Insights from Oman Drilling Project Hole BT1B and preliminary reaction path model approach, paper presented at AGU Fall meeting.

del Real, P. G., Maher, K., Kluge, T., Bird, D. K., Brown, G. E. & John, C. M. (2016). Clumped-isotope thermometry of magnesium carbonates in ultramafic rocks. Geochim Cosmochim Ac, 193, 222-250. https://doi.org/10.1016/j.gca.2016.08.003.

Eiler, J. M. (2007). “Clumped-isotope” geochemistry—The study of naturally-occurring, multiply-substituted isotopologues. Earth and Planetary Science Letters, 262(3), 309-327. https://doi.org/10.1016/j.epsl.2007.08.020.

Emam, A. & Zoheir, B. (2013). Au and Cr mobilization through metasomatism: Microchemical evidence from ore-bearing listvenite, South Eastern Desert of Egypt. Journal of Geochemical Exploration, 125, 34-45. https://doi.org/10.1016/j.gexplo.2012.11.004.

Falk, E. S., Guo, W., Paukert, A. N., Matter, J. M., Mervine, E. M. & Kelemen, P. B. (2016). Controls on the stable isotope compositions of travertine from hyperalkaline springs in Oman: Insights from clumped isotope measurements. Geochim Cosmochim Ac, 192, 1-28. https://doi.org/10.1016/j.gca.2016.06.026.

Falk, E. S. & Kelemen, P. B. (2015). Geochemistry and petrology of listvenite in the Samail ophiolite, Sultanate of Oman: Complete carbonation of peridotite during ophiolite emplacement. Geochim Cosmochim Ac, 160, 70-90. https://doi.org/10.1016/j.gca.2015.03.014.

Gahlan Hisham, A., Azer Mokhles, K. & Asimow Paul, D. (2018). On the relative timing of listwaenite formation and chromian spinel equilibration in serpentinites. American Mineralogist, 103(7), 1087. https://doi.org/10.2138/am-2018-6473.

Ghosh, P., Adkins, J., Affek, H., Balta, B., Guo, W., Schauble, E. A., Schrag, D. & Eiler, J. M. (2006). $^{13}C–^{18}O$ bonds in carbonate minerals: A new kind of paleothermometer. Geochim Cosmochim Ac, 70(6), 1439-1456. https://doi.org/10.1016/j.gca.2005.11.014.

Gnos, E. (1998). Peak metamorphic conditions of garnet amphibolites beneath the Semail Ophiolite: Implications for an inverted pressure gradient. International Geology Review, 40(4), 281-304. https://doi.org/10.1080/00206819809465210.

Gránásy, L., Pusztai, T., Tegze, G., Warren, J. A. & Douglas, J. F. (2005). Growth and form of spherulites. Physical Review E, 72(1), 011605. https://doi.org/10.1103/PhysRevE.72.011605.

Hacker, B. R. (1994). Rapid emplacement of young oceanic lithosphere: Argon geochronology of the Oman Ophiolite. Science, 265(5178), 1563-1565. https://doi.org/10.1126/science.265.5178.1563.

Hacker, B. R. & Gnos, E. (1997). The conundrum of Samail: explaining the metamorphic history. Tectonophysics, 279(1), 215-226. https://doi.org/10.1016/S0040-1951(97)00114-5.

Hacker, B. R. & Mosenfelder, J. L. (1996). Metamorphism and deformation along the emplacement thrust of the Samail ophiolite, Oman. Earth and Planetary Science Letters, 144(3), 435-451. https://doi.org/10.1016/S0012-821X(96)00186-0.

Hacker, B. R., Mosenfelder, J. L. & Gnos, E. (1996). Rapid emplacement of the Oman ophiolite: Thermal and geochronologic constraints. Tectonics, 15(6), 1230-1247. https://doi.org/10.1029/96tc01973.

Halls, C. & Zhao, R. (1995). Listvenite and Related Rocks - Perspectives on Terminology and Mineralogy with Reference to an Occurrence at Cregganbaun, Co Mayo, Republic-of-Ireland. Miner Deposita, 30(3-4), 303-313. https://doi.org/10.1007/Bf00196366.

Hansen, L. D., Dipple, G. M., Gordon, T. M. & Kellett, D. A. (2005). Carbonated serpentinite (listwanite) at Atlin, British Columbia: A geological analogue to carbon dioxide sequestration. Can Mineral, 43, 225-239. https://doi.org/10.2113/gscanmin.43.1.225.

Hinsken, T., Brocker, M., Strauss, H. & Bulle, F. (2017). Geochemical, isotopic and geochronological characterization of listvenite from the Upper Unit on Tinos, Cyclades, Greece. Lithos, 282, 281-297. https://doi.org/10.1016/j.lithos.2017.02.019.

Hofmeister, A. M. (1999). Mantle Values of Thermal Conductivity and the Geotherm from Phonon Lifetimes. Science, 283(5408), 1699-1706. https://doi.org/10.1126/science.283.5408.1699.

Horita, J. (2014). Oxygen and carbon isotope fractionation in the system dolomite–water–CO_2 to elevated temperatures. Geochim Cosmochim Ac, 129, 111-124. https://doi.org/10.1016/j.gca.2013.12.027.

Huntington, K. W., et al. (2009). Methods and limitations of 'clumped' CO_2 isotope (Δ_{47}) analysis by gas-source isotope ratio mass spectrometry. Journal of Mass Spectrometry, 44(9), 1318-1329. https://doi.org/10.1002/jms.1614.

Jaupart, C., Labrosse, S., Lucazeau, F. & Mareschal, J. C. (2015), Temperatures, Heat, and Energy in the Mantle of the Earth, in Treatise on Geophysics (Second Edition), edited by G. Schubert, pp. 223-270, Elsevier, Oxford. https://doi.org/10.1016/B978-0-444-53802-4.00126-3.

Kele, S., et al. (2015). Temperature dependence of oxygen- and clumped isotope fractionation in carbonates: A study of travertines and tufas in the 6–95°C temperature range. Geochim Cosmochim Ac, 168, 172-192. https://doi.org/10.1016/j.gca.2015.06.032.

Kelemen, P. B., et al. (2017), Peridotite carbonation at the leading edge of the mantle wedge: OmDP Site BT1, paper presented at AGU Fall Meeting.

Kelemen, P. B., Kikawa, E. & Miller, J. (2004). Drilling mantle peridotite along the Mid-Atlantic Ridge from 14° to 16°N. Proceedings of the Ocean Drilling Program, Initial Reports (Ocean Drilling Program, College Station, TX), 209, 1-139.

Kelemen, P. B. & Matter, J. (2008). In situ carbonation of peridotite for CO_2 storage. P Natl Acad Sci USA, 105(45), 17295-17300. https://doi.org/10.1073/pnas.0805794105.

Kelemen, P. B., Matter, J., Streit, E. E., Rudge, J. F., Curry, W. B. & Blusztajn, J. (2011). Rates and mechanisms of mineral carbonation in peridotite: natural processes and recipes for enhanced, in situ CO_2 capture and storage. Annu Rev Earth Pl Sc, 39, 545-576. https://doi.org/10.1146/annurev-earth-092010-152509.

Kelemen, P. B., Matter, J. M. & Teagle, D. M. (2014), Scientific Drilling in the Samail Ophiolite, Sultanate of Oman. Grant proposal., edited.

Kelemen, P. B., Matter, J. M., Teagle, D. M. H., Coggon, J. A. & the Oman Drilling Project Science Party (2019). Initial results. In preparation.

Klein, F. & Garrido, C. J. (2011). Thermodynamic constraints on mineral carbonation of serpentinized peridotite. Lithos, 126(3), 147-160. https://doi.org/10.1016/j.lithos.2011.07.020.

Klein, F. & McCollom, T. M. (2013). From serpentinization to carbonation: New insights from a CO_2 injection experiment. Earth and Planetary Science Letters, 379, 137-145. https://doi.org/10.1016/j.epsl.2013.08.017.

Lacinska, A. M. & Styles, M. T. (2012). Silicified serpentinite – a residuum of a Tertiary palaeo-weathering surface in the United Arab Emirates. Geological Magazine, 150(3), 385-395. https://doi.org/10.1017/S0016756812000325.

Lacinska, A. M., Styles, M. T. & Farrant, A. R. (2014). Near-surface diagenesis of ophiolite-derived conglomerates of the Barzaman Formation, United Arab Emirates: a natural analogue for permanent CO_2 sequestration via mineral carbonation of ultramafic rocks. Geological Society, London, Special Publications, 392(1), 343-360. https://doi.org/10.1144/sp392.18.

Lanphere, M. A. (1981). K-Ar ages of metamorphic rocks at the base of the Samail Ophiolite, Oman. Journal of Geophysical Research: Solid Earth, 86(B4), 2777-2782. https://doi.org/10.1029/JB086iB04p02777.

Launay, J. & Fontes, J.-F. (1985). Les sources thermales de Prony (Nouvelle-Calédonie) et leurs précipités chimiques. Exemple de formation de brucite primaire. Géologie de la France, 1, 83-100.

Lewis, T. J., Bentkowski, W. H., Davis, E. E., Hyndman, R. D., Souther, J. G. & Wright, J. A. (1988). Subduction of the Juan de Fuca Plate: Thermal consequences. Journal of Geophysical Research: Solid Earth, 93(B12), 15207-15225. https://doi.org/10.1029/JB093iB12p15207.

Matthews, A. & Katz, A. (1977). Oxygen isotope fractionation during the dolomitization of calcium carbonate. Geochim Cosmochim Ac, 41(10), 1431-1438. https://doi.org/10.1016/0016-7037(77)90249-6.

Meckler, A. N., Ziegler, M., Millán, M. I., Breitenbach, S. F. M. & Bernasconi, S. M. (2014). Long-term performance of the Kiel carbonate device with a new correction scheme for clumped isotope measurements. Rapid Communications in Mass Spectrometry, 28(15), 1705-1715. https://doi.org/10.1002/rcm.6949.

Menzel, M. D., Garrido, C. J., López Sánchez-Vizcaíno, V., Marchesi, C., Hidas, K., Escayola, M. P. & Delgado Huertas, A. (2018). Carbonation of mantle peridotite by CO_2-rich fluids: the formation of listvenites in the Advocate ophiolite complex (Newfoundland, Canada). Lithos, 323, 238-261. https://doi.org/10.1016/j.lithos.2018.06.001.

Menzies, C. D., Wright, S. L., Craw, D., James, R. H., Alt, J. C., Cox, S. C., Pitcairn, I. K. & Teagle, D. A. H. (2018). Carbon dioxide generation and drawdown during active orogenesis of siliciclastic rocks in the Southern Alps, New Zealand. Earth and Planetary Science Letters, 481, 305-315. https://doi.org/10.1016/j.epsl.2017.10.010.

Mervine, E. M., Humphris, S. E., Sims, K. W. W., Kelemen, P. B. & Jenkins, W. J. (2014). Carbonation rates of peridotite in the Samail Ophiolite, Sultanate of Oman, constrained through ^{14}C dating and stable isotopes. Geochim Cosmochim Ac, 126, 371-397. https://doi.org/10.1016/j.gca.2013.11.007.

Müller, I. A., Fernandez, A., Radke, J., van Dijk, J., Bowen, D., Schwieters, J. & Bernasconi, S. M. (2017a). Carbonate clumped isotope analyses with the long-integration dual-inlet (LIDI) workflow: scratching at the lower sample weight boundaries. Rapid Communications in Mass Spectrometry, 31(12), 1057-1066. https://doi.org/10.1002/rcm.7878.

Müller, I. A., Rodriguez-Blanco, J. D., Storck, J.-C., do Nascimento, G. S., Bontognali, T. R. R., Vasconcelos, C., Benning, L. G. & Bernasconi, S. M. (2019). Calibration of the oxygen and clumped isotope thermometers for (proto-)dolomite based on synthetic and natural carbonates. Chem Geol, 525, 1-17. https://doi.org/10.1016/j.chemgeo.2019.07.014.

Müller, I. A., Violay, M. E. S., Storck, J.-C., Fernandez, A., van Dijk, J., Madonna, C. & Bernasconi, S. M. (2017b). Clumped isotope fractionation during phosphoric acid digestion of carbonates at 70°C. Chem Geol, 449, 1-14. https://doi.org/10.1016/j.chemgeo.2016.11.030.

Murray, S. T., Arienzo, M. M. & Swart, P. K. (2016). Determining the Δ_{47} acid fractionation in dolomites. Geochim Cosmochim Ac, 174, 42-53. https://doi.org/10.1016/j.gca.2015.10.029.

Nasir, S., Al Sayigh, A. R., Al Harthy, A., Al-Khirbash, S., Al-Jaaldi, O., Musllam, A., Al-Mishwat, A. & Al-Bu'saidi, S. (2007). Mineralogical and geochemical characterization of listwaenite from the Semail Ophiolite, Oman. Chem Erde-Geochem, 67(3), 213-228. https://doi.org/10.1016/j.chemer.2005.01.003.

Neal, C. & Stanger, G. (1983). Hydrogen generation from mantle source rocks in Oman. Earth and Planetary Science Letters, 66, 315-320. https://doi.org/10.1016/0012-821X(83)90144-9.

Neal, C. & Stanger, G. (1985), Past and present serpentinisation of ultramafic rocks; an example from the Semail ophiolite nappe of northern Oman, in The Chemistry of Weathering, edited by J. I. Drever, pp. 249-275, Springer Netherlands. https://doi.org/10.1007/978-94-009-5333-8.

Nicolas, A. & Boudier, F. (1995). Mapping oceanic ridge segments in Oman ophiolite. Journal of Geophysical Research: Solid Earth, 100(B4), 6179-6197. https://doi.org/10.1029/94jb01188.

Northrop, D. A. & Clayton, R. N. (1966). Oxygen-Isotope Fractionations in Systems Containing Dolomite. The Journal of Geology, 74(2), 174-196. https://doi.org/10.1086/627153.

Osako, M., Yoneda, A. & Ito, E. (2010). Thermal diffusivity, thermal conductivity and heat capacity of serpentine (antigorite) under high pressure. Physics of the Earth and Planetary Interiors, 183(1), 229-233. https://doi.org/10.1016/j.pepi.2010.07.005.

Passey, B. H. & Henkes, G. A. (2012). Carbonate clumped isotope bond reordering and geospeedometry. Earth and Planetary Science Letters, 351-352, 223-236. https://doi.org/10.1016/j.epsl.2012.07.021.

Paukert, A. N., Matter, J. M., Kelemen, P. B., Shock, E. L. & Havig, J. R. (2012). Reaction path modeling of enhanced in situ CO_2 mineralization for carbon sequestration in the peridotite of the Samail Ophiolite, Sultanate of Oman. Chem Geol, 330, 86-100. https://doi.org/10.1016/j.chemgeo.2012.08.013.

Pearce, M. A., Timms, N. E., Hough, R. M. & Cleverley, J. S. (2013). Reaction mechanism for the replacement of calcite by dolomite and siderite: implications for geochemistry, microstructure and porosity evolution during hydrothermal mineralisation. Contrib Mineral Petr, 166(4), 995-1009. https://doi.org/10.1007/s00410-013-0905-2.

Plümper, O., Botan, A., Los, C., Liu, Y., Malthe-Sørenssen, A. & Jamtveit, B. (2017a). Fluid-driven metamorphism of the continental crust governed by nanoscale fluid flow. Nature Geoscience, 10, 685. https://doi.org/10.1038/ngeo3009.

Plümper, O., King, H. E., Geisler, T., Liu, Y., Pabst, S., Savov, I. P., Rost, D. & Zack, T. (2017b). Subduction zone forearc serpentinites as incubators for deep microbial life. Proceedings of the National Academy of Sciences, 201612147. https://doi.org/10.1073/pnas.1612147114.

Quesnel, B., Gautier, P., Boulvais, P., Cathelineau, M., Maurizot, P., Cluzel, D., Ulrich, M., Guillot, S., Lesimple, S. & Couteau, C. (2013). Syn-tectonic, meteoric water-derived carbonation of the New Caledonia peridotite nappe. Geology, 41(10), 1063-1066. https://doi.org/10.1130/G34531.1.

Rioux, M., Bowring, S., Kelemen, P., Gordon, S., Dudás, F. & Miller, R. (2012). Rapid crustal accretion and magma assimilation in the Oman-U.A.E. ophiolite: High precision U-Pb zircon geochronology of the gabbroic crust. Journal of Geophysical Research: Solid Earth, 117(B7). https://doi.org/10.1029/2012JB009273.

Rioux, M., Bowring, S., Kelemen, P., Gordon, S., Miller, R. & Dudás, F. (2013). Tectonic development of the Samail ophiolite: High-precision U-Pb zircon geochronology and Sm-Nd isotopic constraints on crustal growth and emplacement. Journal of Geophysical Research: Solid Earth, 118(5), 2085-2101. https://doi.org/10.1002/jgrb.50139.

Rioux, M., Garber, J., Bauer, A., Bowring, S., Searle, M., Kelemen, P. & Hacker, B. (2016). Synchronous formation of the metamorphic sole and igneous crust of the Semail ophiolite: New constraints on the tectonic evolution during ophiolite formation from high-precision U–Pb zircon geochronology. Earth and Planetary Science Letters, 451, 185-195. https://doi.org/10.1016/j.epsl.2016.06.051.

Rosenbaum, J. & Sheppard, S. M. F. (1986). An isotopic study of siderites, dolomites and ankerites at high temperatures. Geochim Cosmochim Ac, 50(6), 1147-1150. https://doi.org/10.1016/0016-7037(86)90396-0.

Ryb, U., Lloyd, M. K., Stolper, D. A. & Eiler, J. M. (2017). The clumped-isotope geochemistry of exhumed marbles from Naxos, Greece. Earth and Planetary Science Letters, 470, 1-12. https://doi.org/10.1016/j.epsl.2017.04.026.

Schauble, E. A., Ghosh, P. & Eiler, J. M. (2006). Preferential formation of ^{13}C–^{18}O bonds in carbonate minerals, estimated using first-principles lattice dynamics. Geochim Cosmochim Ac, 70(10), 2510-2529. https://doi.org/10.1016/j.gca.2006.02.011.

Schindelin, J., et al. (2012). Fiji: an open-source platform for biological-image analysis. Nature Methods, 9, 676. https://doi.org/10.1038/nmeth.2019.

Schmidt, M., Xeflide, S., Botz, R. & Mann, S. (2005). Oxygen isotope fractionation during synthesis of CaMg-carbonate and implications for sedimentary dolomite formation. Geochim Cosmochim Ac, 69(19), 4665-4674. https://doi.org/10.1016/j.gca.2005.06.025.

Searle, M. P. & Malpas, J. (1980). Structure and metamorphism of rocks beneath the Semail ophiolite of Oman and their significance in ophiolite obduction. Transactions of the Royal Society of Edinburgh: Earth Sciences, 71(4), 247-262. https://doi.org/10.1017/S0263593300013614.

Searle, M. P., Waters, D. J., Garber, J. M., Rioux, M., Cherry, A. G. & Ambrose, T. K. (2015). Structure and metamorphism beneath the obducting Oman ophiolite: Evidence from the Bani Hamid granulites, northern Oman mountains. Geosphere, 11(6), 1812-1836. https://doi.org/10.1130/GES01199.1.

Shtukenberg, A. G., Punin, Y. O., Gunn, E. & Kahr, B. (2012). Spherulites. Chemical Reviews, 112(3), 1805-1838. https://doi.org/10.1021/cr200297f.

Soret, M., Agard, P., Dubacq, B., Plunder, A. & Yamato, P. (2017). Petrological evidence for stepwise accretion of metamorphic soles during subduction infancy (Semail ophiolite, Oman and UAE). Journal of Metamorphic Geology, 35(9), 1051-1080. https://doi.org/10.1111/jmg.12267.

Stanger, G. (1985). Silicified serpentinite in the Semail nappe of Oman. Lithos, 18, 13-22. https://doi.org/10.1016/0024-4937(85)90003-9.

Stowell, H., Zuluaga, C., Boyle, A. & Bulman, G. (2011). Garnet sector and oscillatory zoning linked with changes in crystal morphology during rapid growth, North Cascades, Washington. American Mineralogist, 96(8-9), 1354-1362. https://doi.org/10.2138/am.2011.3759.

Streit, E., Kelemen, P. & Eiler, J. (2012). Coexisting serpentine and quartz from carbonate-bearing serpentinized peridotite in the Samail Ophiolite, Oman. Contrib Mineral Petr, 164(5), 821-837. https://doi.org/10.1007/s00410-012-0775-z.

Sunagawa, I. (2005), Crystals: Growth, Morphology and Perfection, 295 pp., Cambridge Uiversity Press, New York.

Tilton, G. R., Hopson, C. A. & Wright, J. E. (1981). Uranium-lead isotopic ages of the Samail Ophiolite, Oman, with applications to Tethyan ocean ridge tectonics. Journal of Geophysical Research: Solid Earth, 86(B4), 2763-2775. https://doi.org/10.1029/JB086iB04p02763.

Tominaga, M., Beinlich, A., Lima, E. A., Tivey, M. A., Hampton, B. A., Weiss, B. & Harigane, Y. (2017). Multi-scale magnetic mapping of serpentinite carbonation. Nat Commun, 8. https://doi.org/10.1038/s41467-017-01610-4.

Tsikouras, B., Karipi, S., Grammatikopoulos, T. A. & Hatzipanagiotou, K. (2006). Listwaenite evolution in the ophiolite melange of Iti Mountain (continental Central Greece). European Journal of Mineralogy, 18(2), 243-255. https://doi.org/10.1127/0935-1221/2006/0018-0243.

Turcotte, D. & Schubert, G. (2014), Geodynamics, 3 ed., Cambridge University Press, Cambridge, U.K.

van Hinsbergen, D. J. J., Maffione, M., Koornneef, L. M. T. & Guilmette, C. (2019). Kinematic and paleomagnetic restoration of the Semail ophiolite (Oman) reveals subduction initiation along an ancient Neotethyan fracture zone. Earth and Planetary Science Letters, 518, 183-196. https://doi.org/10.1016/j.epsl.2019.04.038.

Warren, C. J., Parrish, R. R., Waters, D. J. & Searle, M. P. (2005). Dating the geologic history of Oman's Semail ophiolite: insights from U-Pb geochronology. Contrib Mineral Petr, 150(4), 403-422. https://doi.org/10.1007/s00410-005-0028-5.

Wilde, A., Simpson, L. & Hanna, S. (2002). Preliminary study of tertiary hydrothermal alteration and platinum deposition in the Oman ophiolite. Journal of the Virtual Explorer, 6, 7-13. https://doi.org/10.3809/jvirtex.2002.00038

Zheng, X., Cordonnier, B., Zhu, W., Renard, F. & Jamtveit, B. (2018). Effects of confinement on reaction-induced fracturing during hydration of periclase. Geochemistry, Geophysics, Geosystems, 19(8), 2661-2672. https://doi.org/10.1029/2017gc007322.

Zheng, Y.-F. (1999). Oxygen isotope fractionation in carbonate and sulfate minerals. Geochemical Journal, 33(2), 109-126. https://doi.org/10.2343/geochemj.33.109.

Supporting Information

- Figures S1 to S4
- Tables S1 to S3

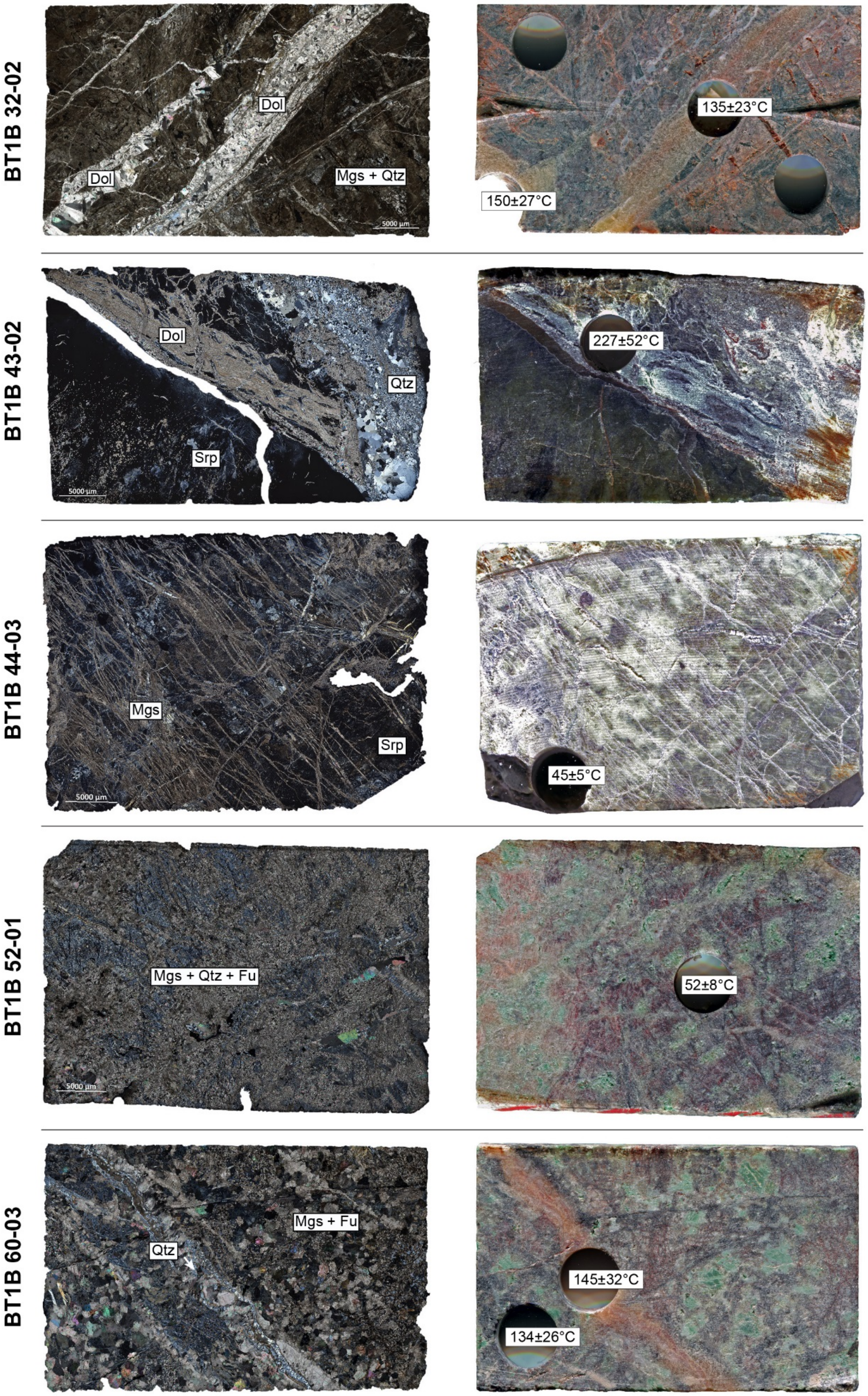
BT1B 32-02
Dol
Dol
Mgs + Qtz
5000 μm
135±23°C
150±27°C
BT1B 43-02
Dol
Qtz
Srp
5000 μm
227±52°C
BT1B 44-03
Mgs
Srp
5000 μm
45±5°C
BT1B 52-01
Mgs + Qtz + Fu
5000 μm
52±8°C
BT1B 60-03
Mgs + Fu
Qtz
145±32°C
134±26°C

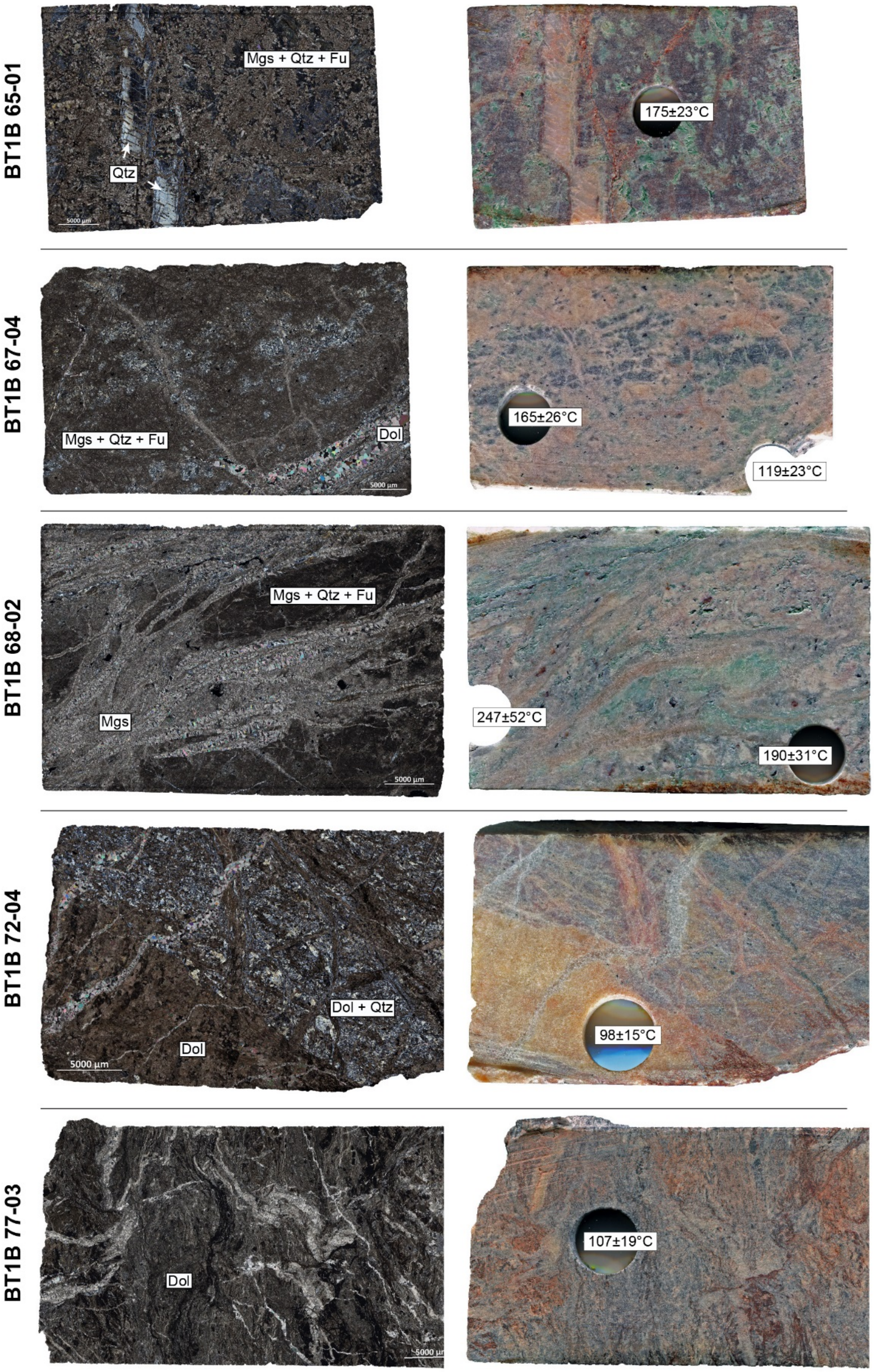

Figure S1 Sampling locations for clumped isotope analyses in all investigated samples. Images on the left side are full thin section scans using cross-polarized light. Images on the right side show the location of micro drill spots in the thin section billets.

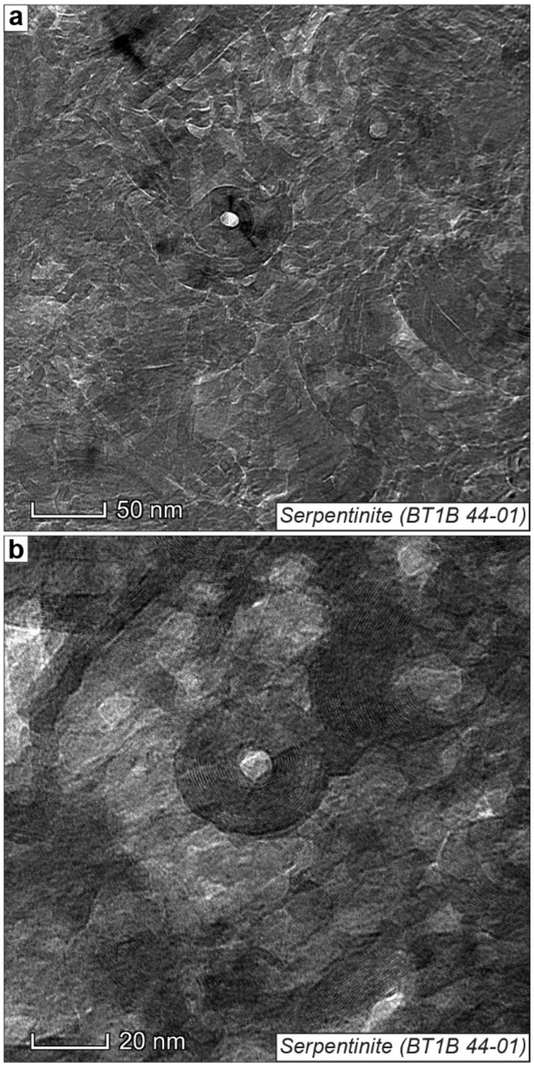

Figure S2 Scanning transmission electron microscope (STEM) bright-field images from sample BT1B 44–01 showing that the serpentine matrix is predominantly composed of lizardite and chrysotile (see also Raman spectrum in Fig. S3).

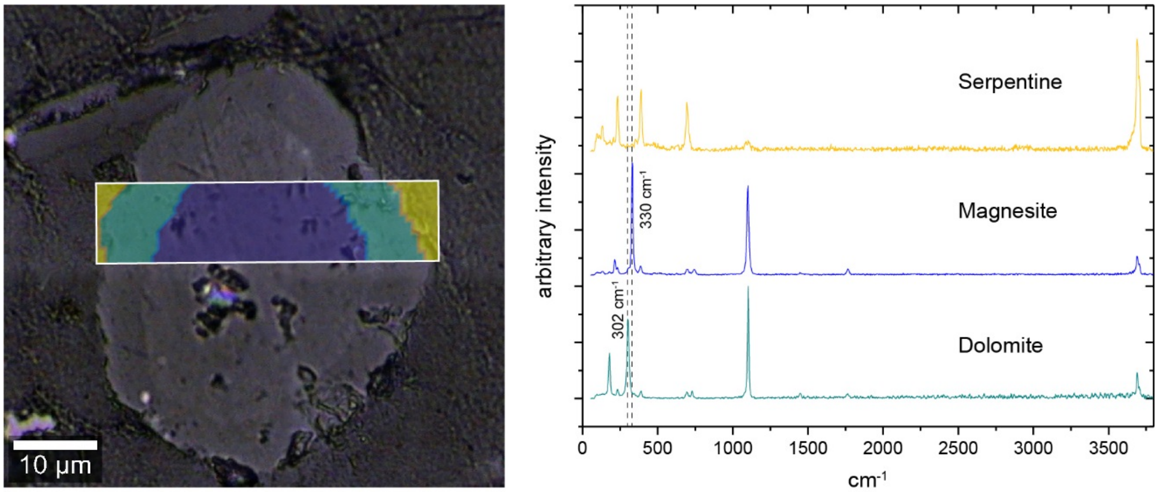

Figure S3 Principal component analysis (PCA) of Raman spectra (left) acquired on a zoned carbonate spheroid in serpentinite sample BT1B 44–01 showing the presence of magnesite in the core surrounded by a thin rim of dolomite in a matrix of chrysotile. Raman spectra (right) are the average spectra for the three zones of the PCA map. Spectra were acquired with a WITec Alpha 300 RA+ at CMCA using the 532 nm laser and a 600 nm/line grating. Raman mapping was carried out at a spatial resolution of 700 nm.

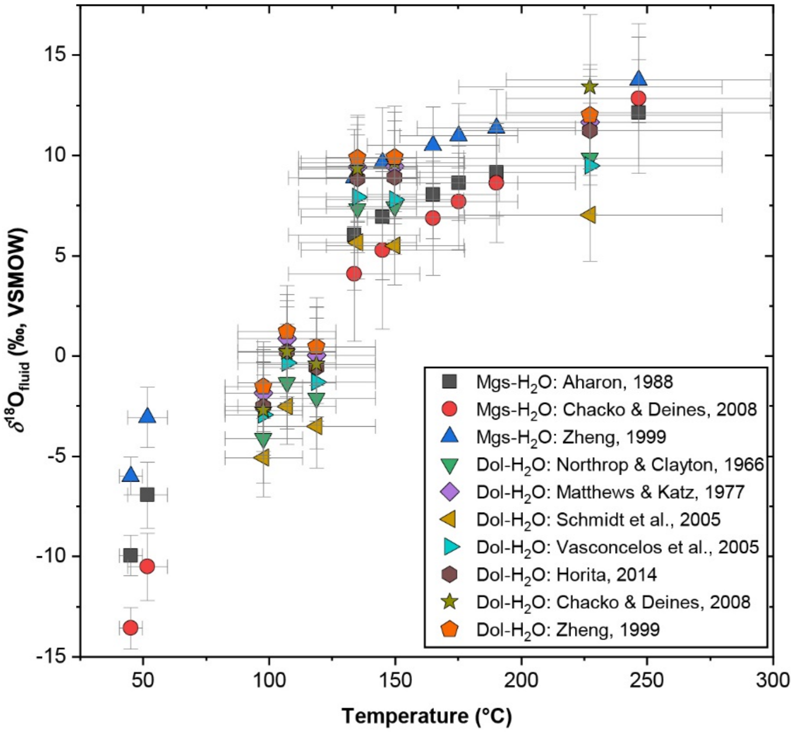

Figure S4 Calculated equilibrium fluid $\delta^{18}O$ (VSMOW) values plotted against carbonate formation temperatures based on various mineral–fluid oxygen isotope fraction factors (see also Fig. 10).

Table S1. Average magnesite composition from selected serpentinite and listvenite samples.

Sample	44-03									72-04						68-02			65-01			60-03				
Description	Matrix Mgs			Matrix Fe-Mgs			Vein Fe-Mgs			Matrix Mgs			Vein Mgs			Vein Mgs			Matrix Mgs			Matrix Mgs			Detection limit	
	Conc.	1σ	n	Conc.	1σ	n	Conc.	1σ	n	Conc.	1σ	n	Conc.	1σ	n	Conc.	1σ	n	Conc.	1σ	n	Conc.	1σ	n	Average	1σ
CaO (wt.%)	0.17	0.06	6	0.72	1.39	8	1.04	0.65	7	0.21	0.11	2	0.30	0.19	7	0.36	0.27	3	0.24	0.08	9	0.35	0.30	13	0.01	0.00
MgO	44.0	0.48	6	29.9	3.73	8	31.6	6.33	7	23.9	2.47	2	38.1	0.68	7	40.5	1.47	3	41.9	2.08	9	42.4	0.81	13	0.01	0.00
FeO	1.78	0.36	6	20.1	5.64	8	17.3	8.27	7	26.6	2.71	2	9.72	0.69	7	7.33	1.51	3	6.49	2.50	9	5.22	0.94	13	0.01	0.00
MnO	1.45	0.59	6	0.08	0.03	8	0.13	0.12	7	0.31	0.01	2	0.10	0.01	7	0.16	0.18	3	0.20	0.24	9	0.06	0.03	13	0.01	0.00
CO_2^*	51.5	0.08	6	47.6	1.21	8	48.2	1.88	7	45.7	0.79	2	50.0	0.14	7	50.5	0.40	3	50.5	0.62	9	50.9	0.30	13		
Total	98.9	0.19	6	98.4	0.29	8	98.2	0.35	7	96.7	0.44	2	98.1	0.37	7	98.8	0.44	3	99.3	0.26	9	98.9	0.49	13		
Sr (μg g^{-1})	340	26	3	327		1	391	128	2	b.d.l.			b.d.l.			278		1	340	25	2	457		1	284	25
Ba	b.d.l.			b.d.l.			371		1	b.d.l.			432		1	b.d.l.			b.d.l.			414		1	317	6
Ce	b.d.l.			b.d.l.			829		1	b.d.l.			b.d.l.			b.d.l.			b.d.l.			b.d.l.			762	10
Pr	b.d.l.			1739		1	1923	757	2	b.d.l.			1217		1	b.d.l.			780		1	1951	920	3	652	6
Sm	733	133	4	b.d.l.			634	117	2	b.d.l.			554	17	2	693		1	767	60	3	678	90	5	531	44
Gd	1290	562	4	885		1	1372	824	3	b.d.l.			965	12	2	b.d.l.			1343	755	3	1165	509	9	488	50
Yb	b.d.l.			b.d.l.			b.d.l.			11245	4231	2	2823	1143	6	2101	790	2	1380	52	2	1686	305	4	978	50
Ca (cpfu)	0.00	0.00		0.01	0.02		0.02	0.01		0.00	0.00		0.00	0.00		0.01	0.00		0.00	0.00		0.01	0.00			
Mg	0.94	0.01		0.69	0.07		0.72	0.11		0.58	0.05		0.84	0.01		0.88	0.03		0.91	0.03		0.92	0.01			
Fe	0.02	0.00		0.26	0.08		0.23	0.11		0.36	0.04		0.12	0.01		0.09	0.02		0.08	0.03		0.06	0.01			
Mn	0.02	0.01		0.00	0.00		0.00	0.00		0.00	0.00		0.00	0.00		0.00	0.00		0.00	0.00		0.00	0.00			
C	1.01	0.00		1.01	0.00		1.01	0.00		1.02	0.00		1.01	0.00		1.01	0.00		1.00	0.00		1.01	0.00			
Total cation	1.99			1.99			1.98			1.97			1.98			1.99			2.00			1.99				

* C assigned stoichiometrically.

Table S2. Average compositions of serpentine and fuchsite.

Sample	44-01				44-03		65-01			
Description	Serpentine after olivine		Serpentine after opx		Serpentine after olivine		Fuchsite		Detection limit	
n	6		7		5		5			
	Conc.	1σ	Conc.	1σ	Conc.	1σ	Conc.	1σ	Average	1σ
SiO_2	44.4	0.31	43.6	0.64	44.8	0.44	51.9	0.84	0.01	0.00
TiO_2	0.03	0.03	0.03	0.06	0.09	0.08	0.06	0.04	0.06	0.00
Al_2O_3	0.15	0.06	0.76	0.38	0.28	0.02	24.6	1.19	0.01	0.00
Cr_2O_3	0.00	0.00	0.45	0.29	0.01	0.01	5.58	0.37	0.04	0.00
FeO	3.09	0.63	6.18	0.76	4.02	0.43	3.43	0.92	0.03	0.00
MnO	0.02	0.04	0.06	0.03	0.04	0.03	0.03	0.06	0.04	0.00
MgO	40.2	0.61	36.4	0.90	38.0	0.99	1.65	0.25	0.01	0.00
CaO	0.06	0.02	0.08	0.02	0.07	0.02	0.38	0.03	0.01	0.00
Na_2O	0.01	0.01	0.01	0.01	0.01	0.01	0.06	0.02	0.01	0.00
K_2O	0.00	0.00	0.00	0.00	0.00	0.00	7.55	0.14	0.01	0.00
NiO	0.23	0.05	0.30	0.10	0.16	0.02	0.15	0.02	0.04	0.00
Cl	0.02	0.01	0.03	0.02	0.02	0.01	0.00	0.00	0.01	0.00
H_2O^*	12.8	0.04	12.7	0.05	12.8	0.01	4.50	0.03		
Total	101.0	0.48	100.5	0.87	100.3	0.99	99.9	0.73		
Si (cpfu)	2.05	0.00	2.05	0.01	2.09	0.00	3.46	0.03		
Ti	0.00	0.00	0.00	0.00	0.00	0.00	0.00	0.00		
Al	0.01	0.00	0.04	0.02	0.02	0.00	1.94	0.07		
Cr	0.00	0.00	0.02	0.01	0.00	0.00	0.29	0.02		
Fe	0.12	0.02	0.24	0.03	0.16	0.02	0.19	0.05		
Mn	0.00	0.00	0.00	0.00	0.00	0.00	0.00	0.00		
Mg	2.77	0.03	2.56	0.04	2.64	0.04	0.16	0.03		
Ca	0.00	0.00	0.00	0.00	0.00	0.00	0.03	0.00		
Na	0.00	0.00	0.00	0.00	0.00	0.00	0.01	0.00		
K	0.00	0.00	0.00	0.00	0.00	0.00	0.64	0.01		
Ni	0.01	0.00	0.01	0.00	0.01	0.00	0.01	0.00		
Cl	0.00	0.00	0.00	0.00	0.00	0.00	0.00	0.00		
O	9.00	0.00	9.00	0.00	9.00	0.00	12.0	0.00		
H	3.96	0.02	3.98	0.03	3.98	0.04	2.00	0.01		
Total cation	8.92	0.01	8.91	0.02	8.89	0.02	8.74	0.04		

* H assigned stoichiometrically.

Table S3. Carbonate stable and clumped isotope data, calculated carbonate formation temperatures and fluid equilibrium oxygen isotope composition.

Sample	Type	Rock	Listvenite type	Mineral	Depth	Δ_{47}		Temperature		$\delta^{13}C_{carbonate}$		$\delta^{18}O_{carbonate}$		$\delta^{18}O_{fluid*}$		
					m	‰	2σ	°C	2σ	‰, VPDB	2σ	‰, VPDB	2σ	‰, VSMOW	2σ	n
32-02	vein	Listvenite	light red	Dol	67.45	0.390	0.032	150	27	0.70	0.02	-7.38	0.44	8.91	2.32	11
32-02	vein	Listvenite	light red	Dol	67.45	0.407	0.029	135	23	0.04	0.02	-6.17	0.20	8.85	2.17	13
43-02	vein	Serpentinite		Dol	94.89	0.324	0.035	227	52	-2.57	0.20	-9.97	0.69	11.24	2.71	14
44-03	vein	Serpentinite		Mgs	98.71	0.548	0.013	45	5	-3.79	0.07	-9.29	0.07	-9.94	1.00	3
52-01	matrix	Listvenite	green	Mgs	118.5	0.531	0.020	52	8	-0.14	0.00	-7.74	0.05	-6.93	1.64	2
60-03	matrix	Listvenite	green	Mgs	141.3	0.379	0.038	134	26	0.01	0.05	-6.91	0.12	6.04	2.74	4
60-03	vein	Listvenite	green	Mgs	141.3	0.366	0.041	145	32	-0.24	0.07	-7.14	0.04	6.94	3.13	5
65-01	matrix	Listvenite	green	Mgs	155.1	0.330	0.025	175	23	0.15	0.13	-8.05	0.25	8.63	1.85	5
67-04	matrix	Listvenite	green	Mgs	163.26	0.341	0.029	165	26	-0.21	0.05	-7.83	0.10	8.04	2.21	4
67-04	vein	Listvenite	green	Dol	163.26	0.429	0.033	119	23	0.06	0.04	-13.77	0.31	-0.58	2.46	13
68-02	matrix	Listvenite	green	Mgs	165.05	0.317	0.031	190	31	0.43	0.07	-8.60	0.13	9.18	2.23	4
68-02	vein	Listvenite	green	Mgs	165.05	0.275	0.035	247	52	0.60	0.04	-9.00	0.14	12.14	2.64	4
72-04	matrix	Listvenite	light red	Dol	178.74	0.461	0.027	98	15	0.47	0.12	-13.35	1.10	-2.52	2.22	9
77-03	matrix	Listvenite	dark red	Dol	193.23	0.446	0.030	107	19	-0.47	0.09	-11.76	0.35	0.22	2.26	11

* Calculated using the fractionation factor from Aharon (1988) for magnesite and Horita (2014) for dolomite.